Continental Shelf Research 30 (2010) 1639–1655

Contents lists available at ScienceDirect

Continental Shelf Research

journal homepage: www.elsevier.com/locate/csr

Observations of submesoscale eddies using high-frequency radar-derived kinematic and dynamic quantities

Sung Yong Kim *

Marine Physical Laboratory, Scripps Institution of Oceanography, University of California, San Diego, La Jolla, CA 92093-0213, USA

ARTICLE INFO

Article history:
Received 2 October 2009
Received in revised form
10 June 2010
Accepted 22 June 2010
Available online 26 June 2010

Keywords:
Submesoscale eddy
Optimal interpolation
High-frequency radar
Surface current
Eddy detection

ABSTRACT

The spatio-temporal variability of submesoscale eddies off southern San Diego is investigated with two-year observations of subinertial surface currents [$O(1)$ m depth] derived from shore-based high-frequency radars. The kinematic and dynamic quantities — velocity potential, stream function, divergence, vorticity, and deformation rates — are directly estimated from radial velocity maps using optimal interpolation. For eddy detection, the winding-angle approach based on flow geometry is applied to the calculated stream function. A cluster of nearly enclosed streamlines with persistent vorticity in time is identified as an eddy. About 700 eddies were detected for each rotation (clockwise and counter-clockwise). The two rotations show similar statistics with diameters in the range of 5–25 km and Rossby number of 0.2–2. They persist for 1–7 days with weak seasonality and migrate with a translation speed of 4–15 cm s^{-1} advected by background currents. The horizontal structure of eddies exhibits nearly symmetric tangential velocity with a maximum at the defined radius of the eddy, non-zero radial velocity due to background flows, and Gaussian vorticity with the highest value at the center. In contrast divergence has no consistent spatial shape. Two episodic events are presented with other in situ data (subsurface current and temperature profiles, and local winds) as an example of frontal-scale secondary circulation associated with drifting submesoscale eddies.

1. Introduction

Vortical phenomena in the ocean are turbulent features that transfer momentum, heat, and oceanic tracers (e.g., temperature, nutrients, and organic matters) through vertical pumping and horizontal propagation (e.g., Munk et al., 2000). Eddies in the open ocean formed dominantly through baroclinic instability of boundary currents and density fronts appear on the scale of the internal Rossby deformation radius. Cyclonic (counter-clockwise herein) eddies are developed around areas of low-pressure and induce upwelling of colder and high-nutrient water. On the other hand, anticyclonic (clockwise) eddies are generated in convergence areas of high-pressure system, and generate downwelling of warmer and nutrient-depleted water, and depress the pycnocline (e.g., Williams and Follows, 1998, 2003). A difference of wind stress at opposite sides of an eddy can induce uneven Ekman transports, which produce maximum vertical velocity at the center of the eddy (e.g., Martin and Richards, 2001; McGillicuddy et al., 2007). Those processes have been observed with high levels of primary production at high-latitudes and near coastal boundaries where wind-driven upwelling is dominant (e.g., Sathyendranath et al., 1995). However, it has been difficult to explain nutrient budgets in new production with only the dynamics of mesoscale eddies, which has raised interest in the missing physical mechanisms (e.g., McGillicuddy et al., 2007; Klein and Lapeyre, 2009).

Submesoscale features, frequently observed as filaments, fronts, and eddies, are characterized by $O(1)$ Rossby number and a horizontal scale smaller than internal Rossby radius of deformation. When a jet along a density front accelerates, a secondary circulation develops in the vertical in the form of upwelling on the warmer side (clockwise eddy) and downwelling on the colder side (counter-clockwise eddy) which are responses to the horizontal density gradient and strain rate (e.g., Woods, 1988; Pollard and Regier, 1990, 1992; Spall, 1995; Williams and Follows, 1998; Capet et al., 2008b; Klein and Lapeyre, 2009). The frontal-scale secondary circulation contributes to the vertical transport of oceanic tracers, mass, and buoyancy and rectifies the mixed layer structure and upper-ocean stratification (e.g., Hoskins and Bretherton, 1972; McWilliams, 1985; Wunsch, 1999; Mahadevan and Tandon, 2006; Capet et al., 2008a; Thomas et al., 2009). Vertical exchanges of tracers are most efficient at the periphery of the submesoscale eddy rather than its center (e.g., Levy et al., 2001). This frontal-scale circulation is found to supply nutrients to the euphotic zone (e.g., Nurser and Zhang, 2000). Thus, frontal scale eddies are related to marine ecosystem and environmental management issues such as biological connectivity and tracking of particles and tracer.

Recent observational and modeling efforts identify contributing forces and factors in the generation of eddies. In other words, the formation of vortical phenomena in the coastal region

* Tel.: +1 858 822 5021; fax: +1 858 534 7132.
E-mail address: syongkim@mpl.ucsd.edu

0278-4343/$ - see front matter © 2010 Elsevier Ltd. All rights reserved.
doi:10.1016/j.csr.2010.06.011

typically results from geophysical factors: effects of bottom bathymetry (e.g., Zimmerman, 1981), headlands (e.g., Signell and Geyer, 1991; Davies et al., 1995; Pawlak et al., 2003), islands (e.g., Wolanski et al., 1984; Pattiaratchi et al., 1986; Ingram and Chu, 1987), unevenly distributed wind (e.g., Oey, 1996; Chavanne et al., 2002), and horizontal shear currents (e.g., Bonnet and Glauser, 1993; Shapiro et al., 1997). In southern California the headlands, islands, and canyons produce complex circulation including persistent vortical phenomena (e.g., DiGicomo and Holt, 2001; Caldeira et al., 2005; Roughan et al., 2005). Oey et al. (2001) described flow dynamics due to wind, pressure gradient, and inertial forcing inferred from numerical model results in the Santa Barbara Channel (SBC). Beckenbach and Washburn (2004) showed westward translation of an oppositely rotating eddy pair in the SBC, and interpreted it as an influence of coastally trapped waves or alongshore currents. In spite of relatively weak wind off southern California, Caldeira et al. (2005) reported island wakes driven by the alongshore wind and California countercurrent. Roughan et al. (2005) proposed that local upwelling off southern San Diego was dominantly driven by flows sliding over headland and their divergence rather than local wind forcing. Although the formation and evolution of eddies in the coastal region have been studied, continuous observation can elucidate the link from coast to offshore and complicated generation mechanisms.

Numerous techniques for identification and classification of two- and three-dimensional vortices have been developed with physical and geometrical criteria (e.g., Jeong and Hussain, 1995; Sujudi, 1995; Portela, 1997; Sadarjoen, 1999). As a physical criterion, Okubo–Weiss (OW) criterion (Okubo, 1970; Weiss, 1981), also called the velocity gradient tensor or the rate of deformation tensor, has been applied to detect surface eddies (e.g., McWilliams, 1984; Isern-Fontanet et al., 2004, 2006; Morrow et al., 2004; Chelton et al., 2007; Chaigneau et al., 2008). On the other hand, geometric criteria have been also used widely in identifying vortical flow pattern: winding-angle (WA) method (e.g., Sadarjoen and Post, 1999; Sadarjoen, 1999), vector pattern matching (e.g., Heiberg et al., 2003), Clifford convolution (e.g., Ebling and Scheuermann, 2003), feature extraction (e.g., Zhu and Moorhead, 1995; Guo et al., 2004; Guo, 2004), and vector geometry (Nencioli et al., 2010). The OW and WA methods are considered to be the primary techniques in the literature of eddy detection, and their comparison has been addressed elsewhere (e.g., Basdevant and Philipovitch, 1994; Chaigneau et al., 2008).

Two-dimensional dynamic ocean surface fields (e.g., surface currents, stream function, and velocity potential) in numerical models and observations have been addressed with finite-difference approximations (e.g., Hubertz et al., 1972; Bijlsma et al., 1986; Li et al., 2006) and normal/open mode analysis (e.g., Cho et al., 1998; Beckenbach and Washburn, 2004; Lipphardt Jr. et al., 2000; Kaplan and Lekein, 2007; Lekien and Gildor, 2009). While those approaches characterize the horizontal structure and pattern of dominant modes, they may not allow the horizontal and vertical structures associated with physical forces and boundary conditions (e.g., local pressure setup and bottom bathymetry).

The novelty of this work is to quantify submesoscale eddies and their horizontal structure through statistical analysis of high-resolution ocean surface current observations. Surface kinematic and dynamic quantities are directly calculated from HF radar-derived radial velocity maps using optimal interpolation (OI). Then, submesoscale eddies are identified with an automated eddy detection technique. OI has been used in the estimate of the current vector as an alternative to an un-weighted least-squares fit (see Kim et al., 2008, for more details). OI is a biased estimator and assumes a (continuous) spatial covariance function, derived

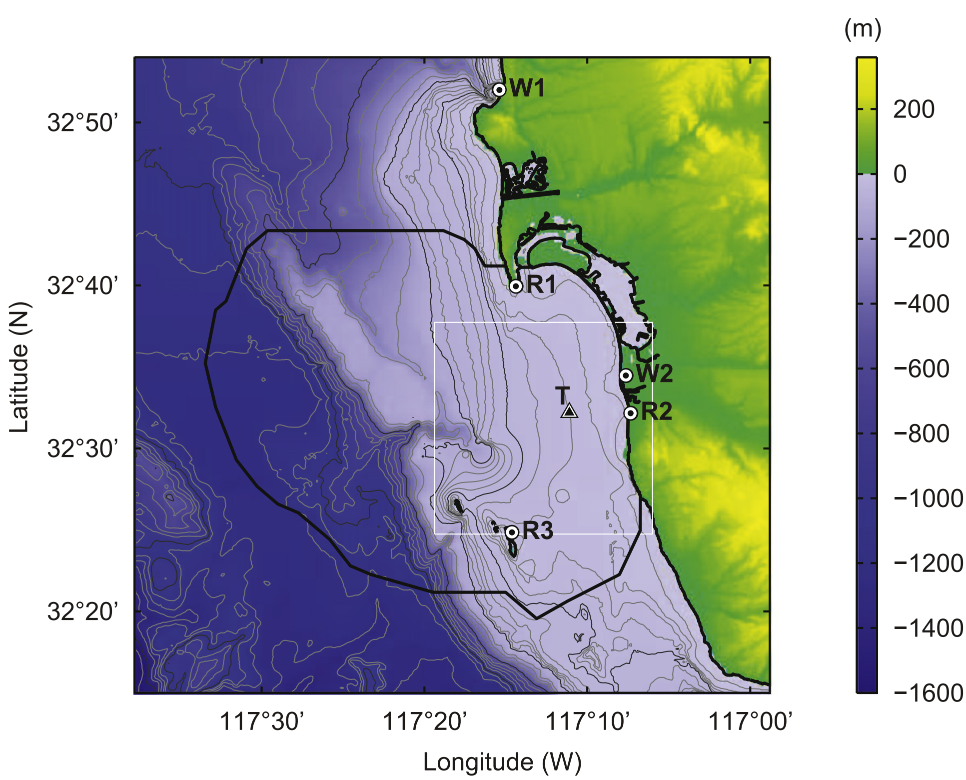

Fig. 1. An observation domain of submesoscale eddies using in situ observations: Three HF radars [R1 (Point Loma), R2 (Imperial Beach), and R3 (Coronado Islands)] for surface currents, two stations at the Scripps Pier (W1, SIO) and Tijuana River Valley (W2, TJR) for wind, and one mooring (T) for both subsurface currents (ADCP) and temperature profile. A black outline denotes the effective coverage area of HF radars (at least 70% data availability for two years). A white square box is the area for closed-up view in Figs. 11a and b. The bottom bathymetry contours are indicated by thin curves with 10 m ($0 < z < 100$ m) and 50 m ($100 < z < 1000$ m) contour intervals and thick curves at the 50, 100, 500, and 1000 m depths.

from the observed spatial scale and structure. It improves both baseline consistency and the uncertainty definition in the estimates. The covariance matrices for OI can be estimated from the normal mode expansion (Section 2 and Appendix A). In addition, this study provides a full description of the technical background of HF radar-derived surface current products.

Besides surface currents measured by HF radars, several in situ observations are used to investigate submesoscale eddies: a single mooring for profiles of subsurface currents (ADCP) and temperature located at T (28 m depth) in Fig. 1. The effective spatial coverage area where three short-range HF radars ($\sim$25 MHz) returned data at least 70% of the time for two years (April 2003–March 2005) is shown as a black curve (approximately 40 km $\times$ 40 km). The data availability of surface currents used in this analysis was shown elsewhere (Fig. 3 in Kim et al., 2007). However, both ADCP and temperature string data are only available for four months (September 2003–February 2004). Thus the vertical structure of the water column related to submesoscale eddies is examined using several episodic events rather than statistical analysis (Section 4.4.2). In this analysis, the stream function is used to identify vortices (e.g., Woods, 1980). A cluster of nearly closed streamlines is an eddy when persistent vorticity is maintained at its center for at least one day. The vorticity is referred to as the relative vorticity.

This paper is composed of four parts. The direct estimates of HF radar-derived kinematic and dynamic quantities using OI are described (Section 2). Then, the applied technique and procedure for detecting eddies are discussed (Section 3). The statistics of detected eddies including horizontal structure within the eddy and the vertical structure from two episodic events are presented in Section 4. The concluding remarks and discussion are in Section 5.

2. Estimate of kinematic and dynamic quantities

The desired kinematic and dynamic quantities from HF radar surface current observations are velocity potential, stream function, divergence, vorticity, and deformation rates including strain rate.

2.1. Velocity potential and stream function

From the Helmholtz decomposition[1] of two-dimensional vector field, surface current vectors are decomposed into a sum of vector components of velocity potential (ϕ) and stream function (ψ) (e.g., McWilliams, 1984; Arfken and Weber, 1995; Li et al., 2006):

$$\mathbf{u} = \mathbf{u}_\phi + \mathbf{u}_\psi = \nabla_H \phi + \mathbf{k} \times \nabla_H \psi, \tag{1}$$

where $\mathbf{u} = [u\ \ v]^\dagger$ († denotes the vector transpose). $\mathbf{u}_\phi$ and $\mathbf{u}_\psi$ are current components corresponding to velocity potential and stream function, respectively ($u = u_\phi + u_\psi$, $v = v_\phi + v_\psi$). $\nabla_H = (\partial/\partial x)\mathbf{i} + (\partial/\partial y)\mathbf{j}$ indicates the horizontal spatial derivative.

The concatenated matrix (ξ) of the velocity potential and stream function at the kth regular grid point are estimated from radial velocities ($\mathbf{r}$) within a search radius (see Section 2.3):

$$\hat{\xi} = \mathrm{cov}_{\mathrm{dm}}^\dagger\ \mathrm{cov}_{\mathrm{dd}}^{-1}\mathbf{r}, \tag{2}$$

where $\xi = [\hat{\phi}\ \ \hat{\psi}]^\dagger$

$$(\mathrm{cov}_{\mathrm{dm}})_{ik} = \mathbf{g}_i^\dagger \langle \mathbf{u}_i \xi_k^\dagger \rangle \tag{3}$$

$$= \mathbf{g}_i^\dagger \begin{bmatrix} \langle u_\phi \phi^\dagger \rangle & \langle u_\psi \psi^\dagger \rangle \\ \langle v_\phi \phi^\dagger \rangle & \langle v_\psi \psi^\dagger \rangle \end{bmatrix}_{ik}, \tag{4}$$

$$(\mathrm{cov}_{\mathrm{dd}})_{ij} = \mathbf{g}_i^\dagger \langle \mathbf{u}_i \mathbf{u}_j^\dagger \rangle \mathbf{g}_j + \delta_{ij}\sigma_r^2 \tag{5}$$

$$= \mathbf{g}_i^\dagger \begin{bmatrix} \langle uu^\dagger \rangle & \langle uv^\dagger \rangle \\ \langle vu^\dagger \rangle & \langle vv^\dagger \rangle \end{bmatrix}_{ij} \mathbf{g}_j + \delta_{ij}\sigma_r^2, \tag{6}$$

$\mathbf{g}_i = [\cos\theta_i\ \ \sin\theta_i]^\dagger$, σ_r^2 is the error variance of surface currents, and θ_i is the bearing angle at the ith radial grid point ($\langle \cdot \rangle$ is the expected value, and i and j indicate indices of radial grid points). The data-model covariance matrices ($\mathrm{cov_{dm}}$) between vector components and velocity potential (or stream function) are computed from power spectral density of velocity potential (or stream function) in the wavenumber space. The data-data covariance matrix ($\mathrm{cov_{dd}}$) is the covariance matrix of radial velocities. The parameterization of the data-model and data-data covariance matrices is discussed in Appendix A. In a similar way, the current components corresponding to velocity potential (u_ϕ and v_ϕ) and stream function (u_ψ and v_ψ) are computed.

The normalized uncertainty covariance matrix ($\hat{\boldsymbol{\chi}}$) of the velocity potential and stream function is defined as

$$\hat{\boldsymbol{\chi}} = \mathbf{I} - \mathrm{cov}_{\mathrm{mm}}^{-1}\mathrm{cov}_{\mathrm{dm}}^\dagger\ \mathrm{cov}_{\mathrm{dd}}^{-1}\mathrm{cov}_{\mathrm{dm}}, \tag{7}$$

where $\mathrm{cov_{mm}}$ denotes the model-model covariance matrix of $\hat{\xi}$, and $\mathbf{I}$ is an identity matrix.

2.2. Divergence, vorticity, and deformation rates

Horizontal divergence (δ), vorticity (ζ), shearing deformation rate (ϱ), stretching deformation rate (ς), and strain rate (κ) of surface currents are

$$\delta = \nabla_H \cdot \mathbf{u} = \frac{\partial u}{\partial x} + \frac{\partial v}{\partial y}, \tag{8}$$

$$\zeta = \nabla_H \times \mathbf{u} = \frac{\partial v}{\partial x} - \frac{\partial u}{\partial y}, \tag{9}$$

$$\varrho = \frac{\partial v}{\partial x} + \frac{\partial u}{\partial y}, \tag{10}$$

$$\varsigma = \frac{\partial u}{\partial x} - \frac{\partial v}{\partial y}, \tag{11}$$

$$\kappa = \sqrt{\varrho^2 + \varsigma^2}. \tag{12}$$

The first order spatial derivative of surface currents ($\partial\mathbf{u}/\partial\mathbf{x}$) at the kth regular grid point is directly estimated from radial velocities ($\mathbf{r}$) within the search radius:

$$\frac{\partial \hat{\mathbf{u}}}{\partial \mathbf{x}} = \mathrm{cov}_{\mathrm{dm}}^\dagger\ \mathrm{cov}_{\mathrm{dd}}^{-1}\mathbf{r}, \tag{13}$$

where $\partial\hat{\mathbf{u}}/\partial\mathbf{x} = [\partial\hat{u}/\partial x\ \ \partial\hat{u}/\partial y\ \ \partial\hat{v}/\partial x\ \ \partial\hat{v}/\partial y]^\dagger$,

$$(\mathrm{cov}_{\mathrm{dm}})_{ik} = \mathbf{g}_i^\dagger \frac{\partial}{\partial \mathbf{x}} \langle \mathbf{u}_i \mathbf{u}_k^\dagger \rangle \tag{14}$$

$$= \mathbf{g}_i^\dagger \frac{\partial[\sigma_s^2(x_k,y_k)\rho(\Delta x_{ik},\Delta y_{ik})]}{\partial \mathbf{x}}, \tag{15}$$

$$(\mathrm{cov}_{\mathrm{dd}})_{ij} = \mathbf{g}_i^\dagger \langle \mathbf{u}_i \mathbf{u}_j^\dagger \rangle \mathbf{g}_j + \delta_{ij}\sigma_r^2 \tag{16}$$

$$= \mathbf{g}_i^\dagger \sigma_s^2(x_k,y_k)\rho(\Delta x_{ij},\Delta y_{ij})\mathbf{g}_j + \delta_{ij}\sigma_r^2, \tag{17}$$

$(\Delta x_{ik},\Delta y_{ik}) = (x_i - x_k, y_i - y_k)$, and $(\Delta x_{ij},\Delta y_{ij}) = (x_i - x_j, y_i - y_j)$. σ_s^2 is the signal variances of surface currents, and $\rho(\Delta x,\Delta y)$ denotes the spatial correlation function.

[1] The Hodge decomposition is a differential form of the Helmholtz decomposition in the two-dimensional vector field.

2.3. Examples of parameters

Several parameters and data-model/data-data covariance matrices used in OI need to be determined in advance (Sections 2.1 and 2.2 and Appendix A).

In implementing the OI method, a search radius (d_0), decorrelation length scales (λ_x and λ_y) of the spatial correlation function, signal variance (σ_s^2), data error variance (σ_r^2) are required. The determination of those parameters has partially been discussed in Kim et al. (2008). In this analysis, the surface current variance is assumed to be as $400\,cm^2\,s^{-2}$, and the data error variance as $40\,cm^2\,s^{-2}$. Although both search radius and decorrelation scales can be a spatial function, they are set as a constant for simplicity in the interpretation. An isotropic exponential correlation function with 3 km decorrelation length scales in x- and y-directions and 6 km search radius are applied. The search radius is connected to the computational expense of the inversion of covariance matrices by cutting off the number of participating radial velocities. Thus it is chosen as a range when spatial correlation becomes 0.05. On the other hand, the search radius also can be a function of space (or distance from the coastline), i.e., it can be smaller nearshore and larger offshore. The spatial density of radial velocities acquired from shore-based HF radars tends to be higher nearshore than offshore. The decorrelation length scales determine the smoothness of estimated current fields. The applied exponential correlation function is based on the spatial structure estimated from unbiased surface current data (Kim et al., 2007). However, as the chosen length scale ($\lambda=3$ km) is about 3–10 times less than the real length scale (10–30 km) (Kim et al., 2007), the influence of the correlation function is minimal on the current field and the structure within eddies (Section 4.4.1).

Covariance matrices [Eqs. (3)–(6)] of surface currents are calculated by differentiating covariance matrices of both velocity potential and stream function with respect to wavenumber space (Appendix A). In this normal mode expansion of the covariance matrix, the number of basis functions in wavenumber space (N_x and N_y), the domain size (L_x and L_y), and the spatial resolution in the physical space (δx and δy) are primary parameters. The spatial resolution and domain size are determined by choosing the spectrum and the maximum wavenumber, which is the minimum scale of the desirable kinematic and dynamic quantities to resolve. The domain size should be larger than the search radius. The number of wavenumber in the power spectral density is chosen as 32 in the x- and y-directions ($N_x=N_y=32$) on the square domain ($L_x=L_y=24$ km) of which resolution is 0.25 km ($\delta x=\delta y=0.25$ km). The assumed covariance function allows resolving the variability with the length scale of 1.5–24 km.

3. Eddy detection

In order to estimate the stream function and velocity potential in the subinertial frequency band (Section 2.1), hourly radial velocities at each range and angular bin are averaged using a one-day moving window. Moreover, surface divergence, vorticity, and deformation and strain rates are computed for the same radial velocities (Section 2.2). There are artifacts in radial velocity maps due to an abrupt change and radial discontinuity in the measured beam pattern of SDBP and SDCI sites, respectively (e.g., Kim et al., 2007; Kim, 2009). These artifacts were identified by an ad hoc approach by examining the root-mean-square (rms) of the difference of radial velocities derived from ideal and measured beam patterns from long-term records (e.g., two-year hourly data). Those spurious radial velocities are excluded prior to all calculations made in this analysis, so results are expected to have minimum influence from radar operations and beam pattern error. An excluded azimuthal bin at SDBP site (287° from true north in clockwise) is shown in Fig. B1a.

Vorticity is a first spatial derivative of current components, which can contain more noise and be more sensitive in spatial and temporal changes than the spatial integration (e.g., stream function and velocity potential). In addition, stream function is more useful and convenient to detect both centers and boundaries of eddies. There are, however, cases where the signs of stream function and vorticity are opposite. Therefore vorticity at the center of the eddy is only used to confirm the detected eddies by comparing with the sign of stream function. Discrepancies between divergence and velocity potential can be also treated in a similar way. Joint probability density functions (PDFs) of those quantities at the center of identified eddies are discussed to justify the use of stream function rather than vorticity as a primary eddy proxy (Section 4.5).

3.1. Technique for eddy detection

While an eddy can be classified into three recognizable patterns — repelling spiral, cycle, and attracting spiral (e.g., Wiebel, 2004), this paper focuses on detecting the circular flow pattern using an automated technique. Basdevant and Philipovitch (1994) and Sadarjoen (1999) discussed how physical criteria used in the eddy detection (e.g., OW) could fail and be subjective in the choice of threshold values. Chaigneau et al. (2008) compared results applying WA and OW methods to the geostrophic current field and suggested that the WA method is more advantageous in terms of efficiency and accuracy. In this paper, the WA method is applied to the estimated stream functions. Repelling and attracting spirals as well as other vortical features could be addressed with Lagrangian coherent structure (e.g., Coulliette et al., 2007).

The WA method (e.g., Sadarjoen, 1999) finds nearly closed streamlines with a single rotation (clockwise or counter-clockwise). Each streamline is a set of N line segments, i.e., a polygon, and the sum (Θ) of their exterior angles (θ_k) should be $\pm 2\pi$:

$$\Theta = \sum_{k=0}^{N-1} \theta_k = \sum_{k=0}^{N-1} \angle P_{k-1}P_kP_{k+1}, \tag{18}$$

where $P_{-1}=P_N$ for a closed polygon and P_k denotes a discrete point of the polygon ($k=0,1,\ldots,N$).

3.2. Clustering streamlines in space

Co-centered streamlines with the same rotation (clockwise or counter-clockwise) are clustered. Some eddies can be shrunk and expanded as they migrate, and merged into one or populated into two or more (e.g., Aref, 1983; Higgins et al., 2009). For these cases, clustering streamlines requires a special data structure. For example, when a mother-eddy encloses three child-eddies, four

Table 1
Geometric properties of an eddy.

Variables	Symbols
Center (longitude, latitude)	x, y
Local depth	z
Time	t
Diameter	L
Major and minor axes	a, b
Tilted angle	θ
Eccentricity	ε
Intensity	n

eddies are identified as individuals and the mother-eddy has a pointer of three child-eddies (e.g., Nybelen and Paoli, 2009). However, this study focuses on the census and feature extraction of submesoscale eddies, so dynamics related to the merge and population of eddies will be left for future work.

As defined in previous studies (e.g., McWilliams, 1990; Glenn et al., 1990; Sanderson, 1995; Hwang et al., 2004; Brassington, 2009), the geometric properties for each cluster of streamlines are summarized in Table 1. The principal axes of each cluster are estimated by considering each cluster as a set of points. The center of an eddy (x, y) is the center of the innermost streamline, because when a cluster has non-circular shape, the center of all points in the cluster can be located outside of the outmost streamline. The size of the eddy ($L=\sqrt{4S/\pi}$) is the diameter corresponding to the area of the outermost streamline ($S=\pi ab$). The eccentricity ($\varepsilon = b/a \leq 1$) is computed as the ratio of minor to major axes. The intensity (n) is defined as the number of streamlines in a cluster. The vorticity and divergence [Eq. (9)] are normalized by local Coriolis frequency (f_c). A cluster is flagged if the sign of rotation of both stream function and vorticity at the center are mismatched, and is not included in the statistics described in the following sections. An example describing a sequential procedure from radial velocity maps to ellipse fitting is shown in Appendix B.

3.3. Tracking eddies in time

If a cluster has the same rotation (clockwise or counter-clockwise) on adjacent time steps and the two centers are within a specified drifting range ($r_0 = 1.2$ km), they are considered to be part of eddy time series. This drifting range can be determined by taking into account the typical translation speed of eddies in this region. However, if the outermost streamlines in consecutive time steps overlap over a 50% area, this range can be set up with flexibility (e.g., $r_0 = 2.5$ km). The length of eddy time series, defined as persistence (γ), is used to filter out the noise and error in the observations and an automated eddy detection technique.

4. Results

A threshold persistence (γ_0) is chosen as one day (24 hours) to filter out randomly identified vortical fields. Since the subinertial radial velocity map is computed using a moving average of one-day time windows (Section 3), vortical features are required to last in the non-overlapped data set, i.e., at least one day, in order to be claimed as a persistent eddy field. Although this threshold can eliminate meaningful eddies by chance that may not affect overall statistics in this paper. The number of identified clockwise and counter-clockwise eddies is, respectively, 774 and 705. The results hereafter will be described with those eddies unless explicitly stated otherwise.

4.1. Significant level of eddy detection technique

The significance level of the applied automated detection algorithm is evaluated with randomly shuffled time series of surface current maps in order to randomize phase in time (e.g., Ebisuzaki, 1997). The number of eddies identified from a shuffled data set is zero when the same threshold of persistence and drifting range are applied. Moreover, the significance level is weakly sensitive to the applied criteria in Section 3.

4.2. Statistics of kinematic and dynamic properties

Both clockwise and counter-clockwise eddies have a similar size with a diameter (L) of 5–20 km (Fig. 2a). Since the outmost streamline can be non-elliptical, the ellipse fitting in this study is done on all streamlines within an eddy as shown in Fig. B3. Thus, estimated major (a) and minor (b) axes are 3.6–4 times less than the effect diameter of the outermost streamline (L) in this analysis (not shown):

$$\frac{L}{a}, \frac{L}{b} = 3.6\text{–}4. \tag{19}$$

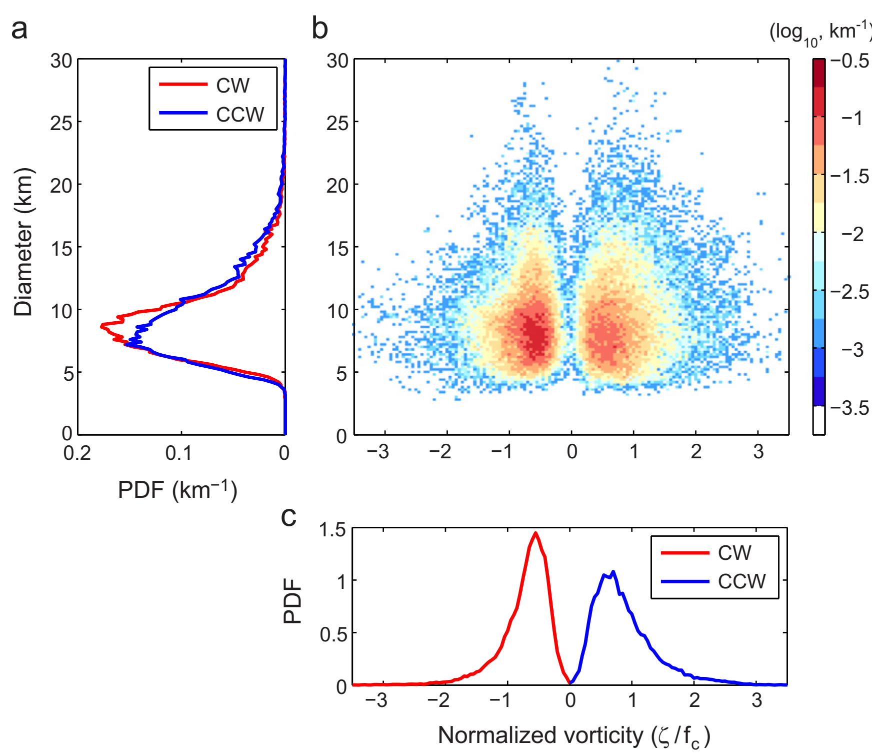

Fig. 2. Probability density functions (PDFs) of (a) diameter (L) and (c) normalized vorticity (ζ/f_c) of eddies. (b) Joint PDF of diameter and normalized vorticity.

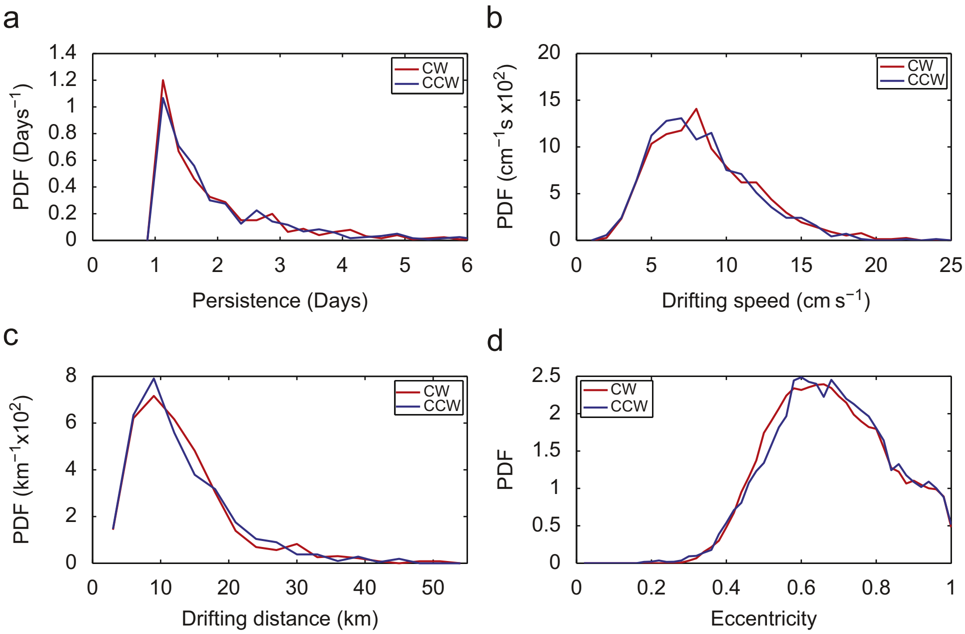

Fig. 3. PDFs of (a) persistence (γ, days), (b) averaged drifting speed (cm s^{-1}), (c) drifting distance (km), and (d) eccentricity of eddies.

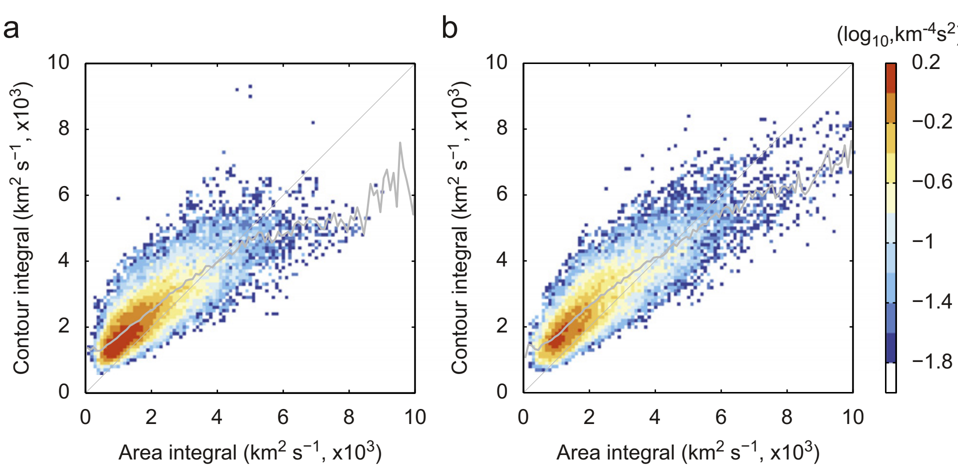

Fig. 4. The line and area integrals on the circulation are presented as their joint PDFs ($\log_{10}$ scale, km^{-4} s^2) for (a) clockwise and (b) counter-clockwise eddies. A black and gray lines indicate the linear relationship [Eqs. (20) and (21)] and the mode at each bin in the area integral axis, respectively.

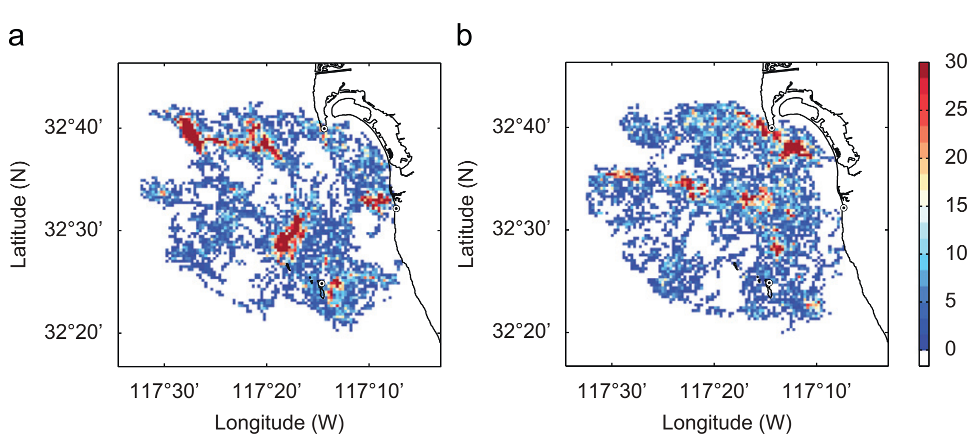

Fig. 5. Spatial distribution of (a) clockwise and (b) counter-clockwise eddies is presented as the number of eddies within a square box (450 m $\times$ 450 m). White space indicates the bin with zero values.

The normalized vorticity (ζ/f_c), which is referred as to Rossby number (R_o), varies between the range of quasi-geostrophic [$O(10^{-1})$] and submesoscale [$O(1)$] (Fig. 2c). The dominant Rossby number of counter-clockwise eddies ($|\zeta/f_c| = 0.7-0.8$) is slightly higher than that of clockwise ones ($|\zeta/f_c| = 0.5-0.6$). The joint PDF of the size and Rossby number present an overview of the submesoscale discussed in this analysis (Fig. 2b). Observed eddies have the effective diameters of 5–15 km and Rossby number of 0.2–1.5.

The persistence, the drifting speed and translation distance, and eccentricity of eddies are shown as PDFs (Fig. 3). In general, clockwise and counter-clockwise eddies have similar statistics on those properties. Most of eddies have at most 6 days persistence and drift over 5–20 km with speeds of 5–15 cm s^{-1}. The eccentricity of fitted ellipses is 0.6–0.7.

Since the applied technique for eddy detection is based on flow geometry, it needs to be examined if circulation (Γ) is conserved within an eddy (Kelvin's circulation theorem, e.g., Hoskins and Bretherton, 1972). Circulations computed in two ways are compared: (1) the piecewise line integral of stream function-derived currents ($\mathbf{u}_\psi$) and (2) the product of an averaged vorticity ($\overline{\zeta}$) and an area of the outermost streamline (S):

$$\Gamma \equiv \oint_C \mathbf{u} \cdot \mathrm{d}\mathbf{l} = \oint_C \mathbf{u}_\psi \, \mathrm{d}l \approx \sum \mathbf{u}_\psi \Delta l, \tag{20}$$

$$\equiv \int\int_S (\nabla \times \mathbf{u}) \cdot \mathrm{d}\mathbf{S} = \int\int_S \overline{\zeta} \cdot \mathrm{d}\mathbf{S} \approx \overline{\zeta} S, \tag{21}$$

where Δl is a piecewise streamline of an eddy.

Both integrals have nearly same order of magnitude (Fig. 4). The vorticity in the solid body is assumed to be isotropic as a function of distance from the center (e.g., linearly decay vorticity from the center). However, the vorticity estimated from observations is likely to be anisotropic and asymmetric, which can cause the difference in two estimates (Fig. 4).

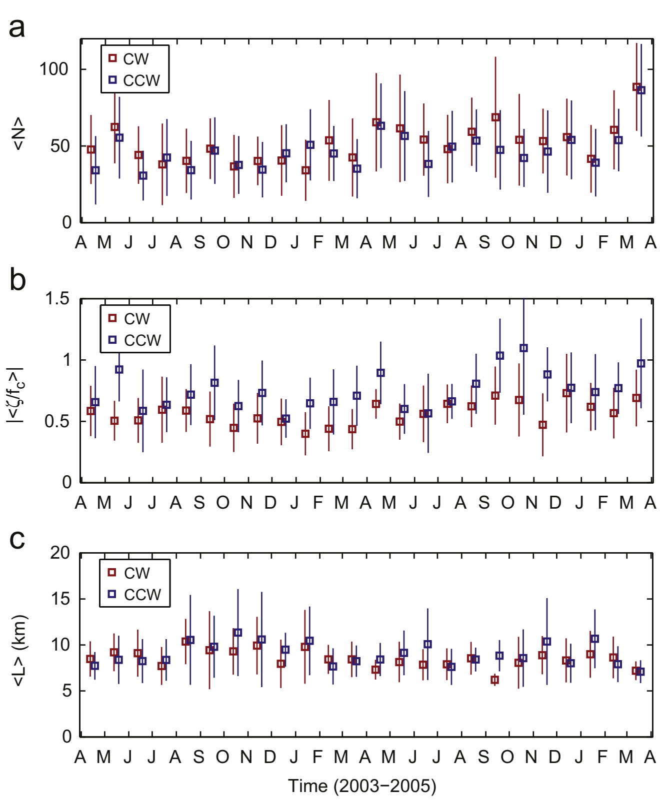

Fig. 6. A time series of the monthly averaged (a) occurrence (N), (b) absolute value of normalized vorticity ($|\zeta/f_c|$), and (c) diameter (L, km) of clockwise (red) and counter-clockwise (blue) eddies. The mean and root-mean-square (rms) are computed using the non-overlapped monthly moving window, and plotted with three-day shift from the center of each month to avoid overlapping. (For interpretation of the references to color in this figure legend, the reader is referred to the web version of this article.)

4.3. Spatial and temporal occurrences

The spatial distribution of eddies exhibits a preferred area in their generation and migration (Fig. 5). Eddies with both rotations are generated near the area south of Point Loma headland and San Diego Bay mouth, where the influence of both coastline and bottom topography become meaningful: clockwise eddies due to the reflection of eastward onshore currents and counter-clockwise eddies due to both interactions between the southward currents rolling over the headland (or at the trailing edge) and northward counter-currents nearshore. Clockwise eddies frequently appear in the center of the domain, the west of the Tijuana River (TJR), and the east of the Coronado Islands. Counter-clockwise eddies are found uniformly along a latitudinal line (32.35°N) as westward/northwestward drifting (or propagating) eddies. About 29% (44%) of clockwise eddies and 42% (61%) of counter-clockwise eddies are found in areas with less than 50 m (100 m) water depth. A spatial histogram of centers of identified eddies in $\sim 450\,\mathrm{m} \times 450\,\mathrm{m}$ bins in Fig. 5, the sum of which sum is equal to total occurrence of eddies.

The occurrence, normalized vorticity, and diameter of eddies are presented as monthly time series in Fig. 6. Those time series are computed using a non-overlapped monthly time window and are plotted with a three-day shift in order to avoid overlapping of error bars. Eddies show weak seasonality with relatively more occurrence in summer than in winter. Typically pairs of eddies with opposite rotations are observed.

Seasonally averaged stream function ($\langle \psi \rangle$) and corresponding surface currents ($\langle \mathbf{u}_\psi \rangle$) are shown in Fig. 7. Seasons are defined as spring (March–May), summer (June–August), fall (September–November), and winter (December–February). Stream functions appear as counter-clockwise onshore (within 20 km from coast) and clockwise offshore with meandering currents. The strength of the stream function changes with season — maximum in spring and minimum in winter when the dominant rotation switches from counter-clockwise to clockwise. However, the occurrence of eddies has weak seasonality. A bifurcated flow near the TJR, frequently observed as a filament or tongue in the satellite remote sensing data, is presented as stream function with opposite sign when the influence of nearshore counter currents becomes dominant in winter. An artifact along an azimuthal bin (287° from true north in clockwise at SDBP) is slightly visible offshore (Fig. B1a).

4.4. Spatial structure

4.4.1. Horizontal structure

The horizontal internal structure of the eddy is examined with radial and tangential velocities, vorticity, and divergence along major and minor axes, presented as a function of relative distance from the center (r/a). Since internal structure along major and minor axes are nearly similar, their shapes on the major axis are only presented (Fig. 8). As mentioned in Section 4.2, the radius of the eddy ($R=L/2$) is approximately twice of major axis, i.e.,

$$\frac{r}{R} \approx \frac{1}{2}\frac{r}{a}. \tag{22}$$

The horizontal current structure is nearly symmetric with small mismatches (5–10%) in positive and negative axes (Fig. 8). The tangential velocity (v_θ) and its rms have maxima around 1.8

for both rotations (Fig. 8a). The radial velocity (v_r) varies within $5\,\mathrm{cm\,s^{-1}}$ (Fig. 8b). The non-zero radial velocity is frequently observed due to background currents (e.g., Beckenbach and Washburn, 2004). The vorticity distribution shows that the counter-clockwise rotation is slightly (0.1–0.2) higher than clockwise one. The magnitude of vorticity has 0.5–0.7 at the center as a maximum and decays near or below zero (Gaussian shape). However, the divergence does not show meaningful structure compared to others, because the intense vertical currents appear at the boundary of eddies as a form of a secondary circulation near the front. Although shearing and stretching deformation rates (ϱ/f_c and ς/f_c) are expected to have the highest variance at the edge of an eddy, i.e., the area near zero vorticity (Mahadevan and Tandon, 2006; Thomas et al., 2009), their horizontal structures do not show the same spatial characteristics (Fig. B4).

Both tangential velocity (v_θ) and angular velocity ($\omega_z = \zeta/2$) of the idealized eddies — Taylor's (Taylor, 1918) and Vatistas' (Vatistas, 1998) vortices — are compared with observations (Figs. 8 and 9). The tangential velocities of two ideal vortices are

$$v_\theta(r) = v_\theta^* \frac{r}{R} \exp\left[\frac{1}{2}\left(1 - \frac{r^2}{R^2}\right)\right] \tag{23}$$

and

$$v_\theta(r) = v_\theta^* \frac{r}{R}\left(1 + \frac{r^4}{R^4}\right)^{-1/2}, \tag{24}$$

where r is the distance from the center and R is the radius of the eddy. v_θ^* is a maximum tangential velocity and the radial velocity is assumed to be zero ($v_r = 0$). The angular velocity $[\omega_z(r) = \partial v_\theta/\partial r]$ is also compared (Figs. 9c and d).

Due to a weak asymmetry of tangential velocities (Fig. 8a), the tangential velocity is normalized with maximum (v_θ^*) in each side of major axis separately. A minor shift of the horizontal axis was made to cross the zero at the center. Since the angular vorticity (ω_z) and data-derived vorticity (ζ/f_c) are not directly comparable quantities due to the normalization with v_θ^*, their shapes near the center are fitted with a constant scale compensating for the magnitude difference. When the data-derived tangential velocity and angular vorticity are fitted to models, the scale of the horizontal axis is adjusted. The tangential velocity is best fit to Taylor's eddy when the axis is scaled up by 1.26 (clockwise) and 1.32 (counter-clockwise) (Figs. 9a and b). On the other hand, the axis of the angular velocity is well fitted to Taylor's eddy when the axis becomes shrunken about 0.7 times for both rotations (Figs. 9c and d) (e.g., McWilliams, 1990).

4.4.2. Vertical structure

An example to show continuity between surface and subsurface currents is shown in Figs. 11 and 12. Two episodic events are chosen when counter-clockwise and clockwise eddies passed a local mooring, giving ADCP and temperature profiles (Figs. 11a and b). Time lines at these two snapshots are indicated as black lines in Figs. 11c–d and 12. The time series of velocity potential (ϕ), stream function (ψ), and normalized divergence (δ/f_c), vorticity (ζ/f_c), shearing deformation rate (ϱ/f_c), stretching deformation rate (ς/f_c), and strain rate (κ/f_c) estimated from HF radar surface current observations at the mooring location for 30 days, centered by two events, are shown in Figs. 11c–e. The positive ($\delta > 0$) and negative ($\delta < 0$) surface divergences denote upwelling and

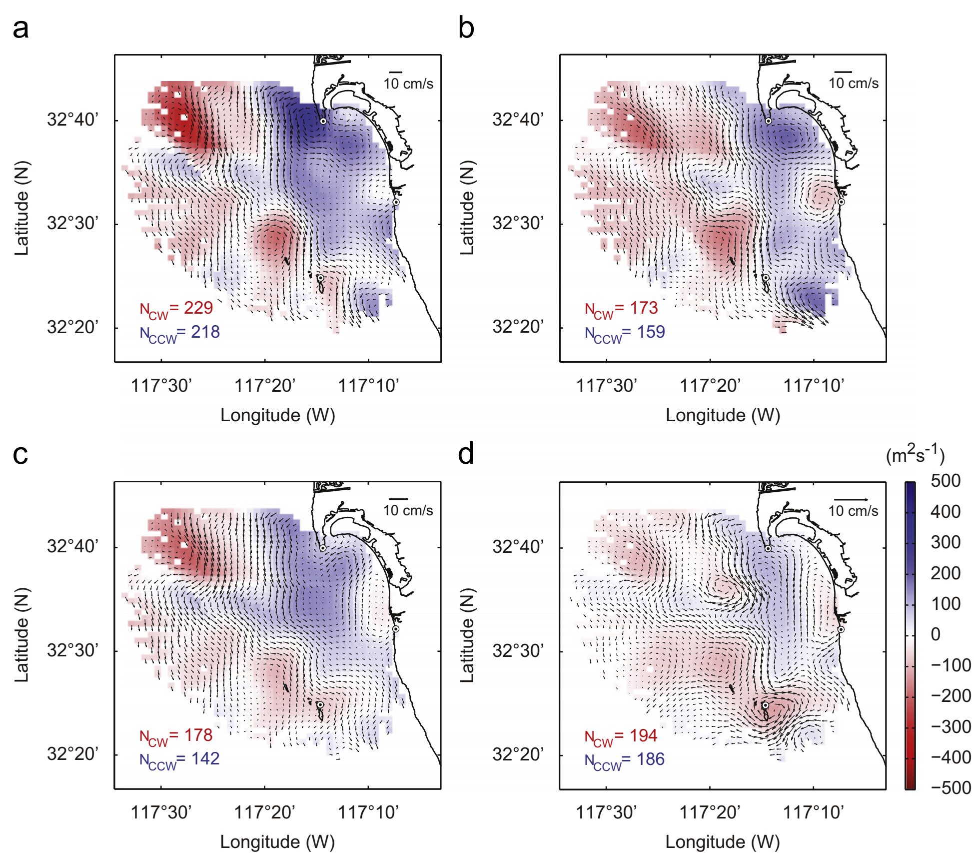

Fig. 7. Seasonally averaged stream function ($\langle\psi\rangle$, $\mathrm{m^2\,s^{-1}}$) and corresponding surface currents ($\langle\mathbf{u}_\psi\rangle$, $\mathrm{cm\,s^{-1}}$). (a) Spring (March–May). (b) Summer (June–August). (c) Fall (September–November). (d) Winter (December–February). The number of identified clockwise (red) and counter-clockwise (blue) eddies in each season is noted. The scale of the current vector differs in each season. (For interpretation of the references to color in this figure legend, the reader is referred to the web version of this article.)

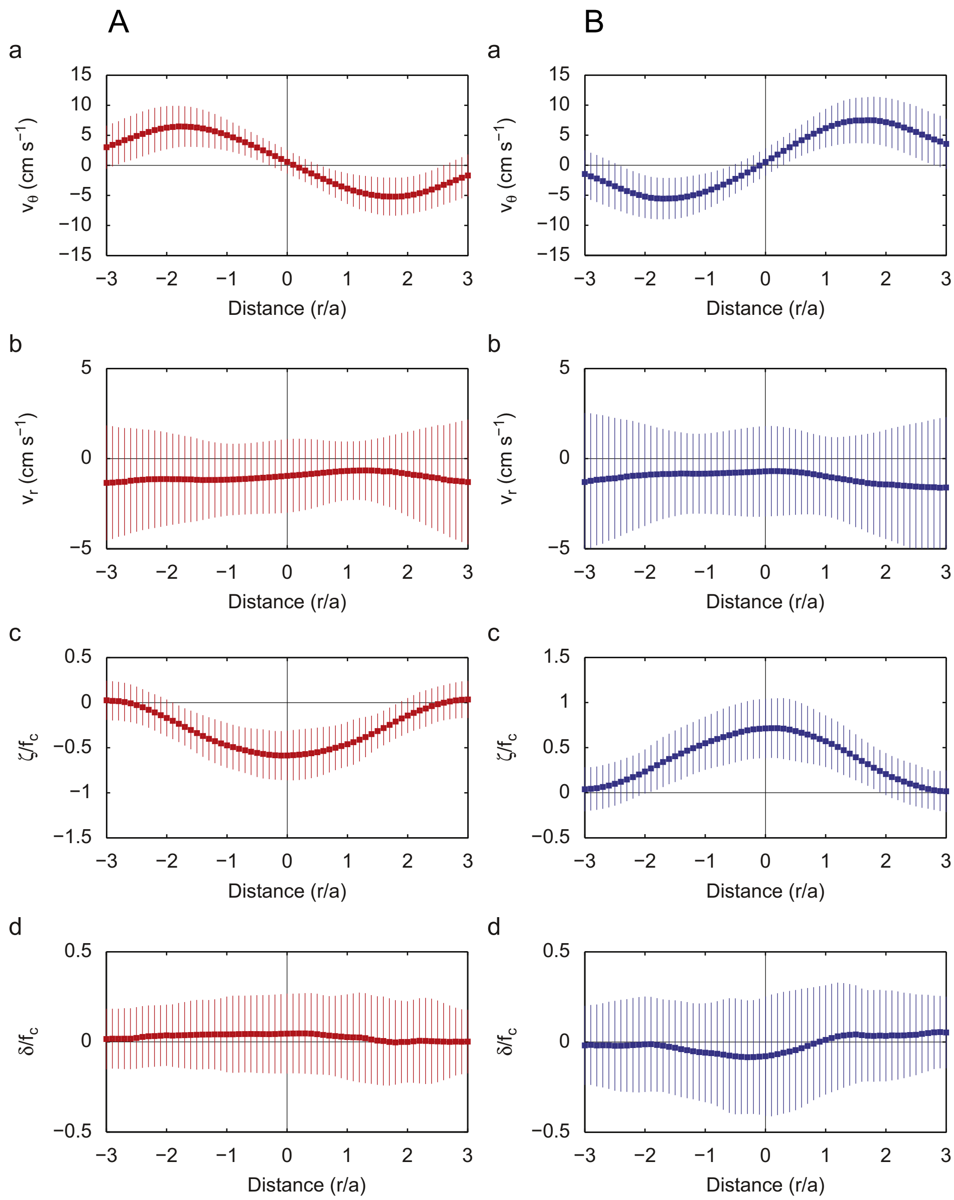

Fig. 8. Horizontal structure of submesoscale eddies along the major axis (r/a) is presented as a function of distance from the center. The mean and rms are indicated as squares and error bars, respectively. Column A: clockwise eddies. Column B: counter-clockwise eddies. (a) Tangential velocity (v_θ). (b) Radial velocity (v_r). (c) Normalized vorticity (ζ/f_c). (d) Normalized divergence (δ/f_c).

downwelling at surface. During the same time period, concurrent subinertial time series of subsurface currents, vertical rotation coefficient [α in Eq. (25)] superposed with normalized stream function ($\psi^* = \psi/\psi_0$, $\psi_0 = 500\,\mathrm{m}^2\,\mathrm{s}^{-1}$), temperature profile, and local winds at SIO and TJR are also examined (Fig. 12a). The HF radar-derived surface currents are overlaid on the top of subsurface currents, which presents vertical continuity between two independent observations (Figs. 12a and b). The linear regression coefficient, skill score, and correlation coefficient between surface currents and current at the few upper bins are reported elsewhere (Kim, 2009).

The vertical rotary coefficient (α) is defined as a function of time (e.g., Leaman and Sanford, 1975; Garrett and Munk, 1979):

$$\alpha(t) = \frac{-\sum_{m<0} S(m,t) + \sum_{m>0} S(m,t)}{\sum_{m<0} S(m,t) + \sum_{m>0} S(m,t)}, \tag{25}$$

where $S(m,t)$ is the rotary power spectrum of vertical current profile at time t and m is the vertical wavenumber. Negative ($\alpha < 0$) and positive ($\alpha > 0$) values indicate clockwise and counter-clockwise (looking down from the top), respectively. While this coefficient can be limited to the vertical resolution and ambiguous to the current profile with a single direction (e.g., uniform flow throughout the water column), it can represent the rotation of water column.

The submesoscale processes are characterized by the intense vertical velocity associated with ageostrophic secondary circulation as a response to horizontal density gradient and strain rate (e.g., Hoskins and Bretherton, 1972; Williams and Follows, 2003; Capet et al., 2008b; Klein and Lapeyre, 2009). Vertical exchanges of tracers are most efficient at the periphery of the eddy, i.e., where the vorticity changes its sign or the strain rate becomes greatest, rather than its center (e.g., Levy et al., 2001; Lapeyre and Klein, 2006; Mahadevan and Tandon, 2006; Mahadevan et al.,

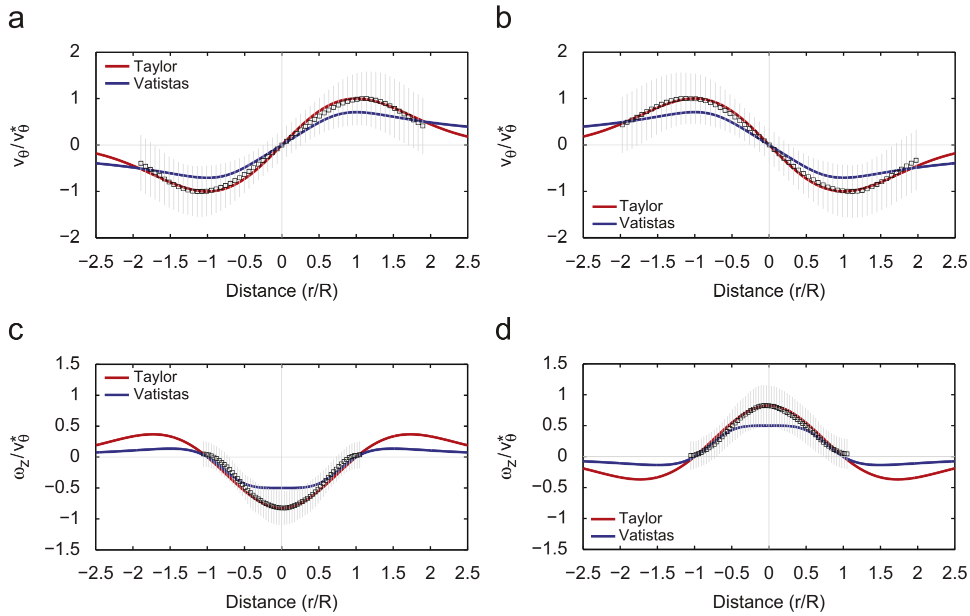

Fig. 9. Horizontal structures of data-derived tangential velocity [v_θ, (a) and (b)] and angular velocity [ω_z, (c) and (d)] normalized by maximum tangential velocity (v_θ^*) are compared with Taylor's and Vatistas' vortices presented as a function of relative distance (r/R) from the center [R is the radius of the eddy]. (a) and (c): Clockwise eddies. (b) and (d): Counter-clockwise eddies. The data-derived tangential velocity and vorticity are fitted into ideal vortices. The mean and rms are shown as the black square with gray line error bar.

2008). However, both areas, where the vorticity changes its sign and the strain rate become high, do not always align.

In order to explain the vertical structure created by drifting submesoscale eddies around a local mooring, a moving density front at the boundary between two surface eddies — a clockwise eddy on the light (warm) side and a counter-clockwise eddy on the heavy (cold) side — is considered (Fig. 10, see Pollard and Regier, 1992; Capet et al., 2008b; Klein and Lapeyre, 2009 for more details]. The vertical secondary circulation (counter-clockwise thick arrows) in the cross-front plane drifts in time as the front does. When the front approaches from $x=0$ to $x=x_a$, the sign of vorticity (or stream function) changes from negative (clockwise) to positive (counter-clockwise). At the same time, a strong upward current ($w>0$) elevates the thermocline, then a downward current pushes it down. However, the downwelling within the counter-clockwise eddy, for example, at the center of the eddy, is not as intense as at the boundary. On the other hand, the front moves from $x=0$ to $x=x_b$, the vorticity sign turns from positive (clockwise) to negative (counter-clockwise) as does the sign of stream function. In the same way, a strong downward current ($w<0$) is followed by a upward current ($w>0$), and the pycnocline fluctuates with frontal-scale vertical velocities.

A clockwise eddy passes by the local mooring between 305 and 310 yeardays from northwest to southeast, followed by a counter-clockwise eddy (Figs. 11c–e). A strong upward current raises up the thermocline (Fig. 12d) when the sign of vorticity (or stream function) changes on 310 (or 311) yeardays from negative to positive (Fig. 11b). At that time, the shearing rate ($\varrho>0$) and stretching rate ($\varsigma<0$) have their local maximum and minimum, respectively, with opposite signs (Fig. 11e). As long as the local mooring is located within the core of the counter-clockwise eddy (Figs. 11a and b), the downward currents continue ($\delta/f_c<0$ and $\zeta/f_c>0$). As an opposite case, a counter-clockwise eddy moves from south to northwest between 321 and 327 yeardays around the mooring (Fig. 11b). The thermocline is pushed down near the timing when stream function and vorticity (positive to negative) change their signs as well as velocity potential and divergence (negative to positive) do on 323.62 yeardays (Fig. 12d). The local high shearing

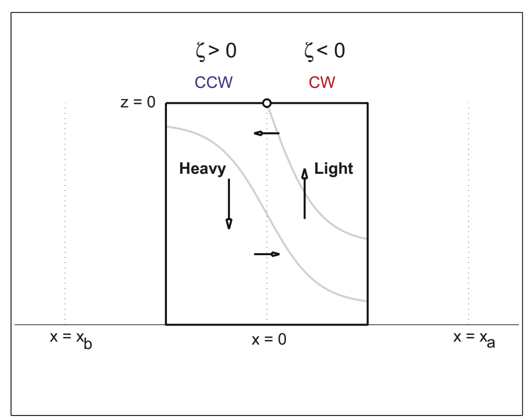

Fig. 10. A schematic frontal-scale secondary circulation associated with a drifting density front (at $x=0$ and $z=0$) presented in the cross-front plane view (adapted from Hoskins and Bretherton, 1972; Pollard and Regier, 1992; Munk et al., 2000; Williams and Follows, 2003). When a jet along the density front accelerates, a secondary circulation develops in vertical as the form of upwelling on the warmer side (clockwise eddy) and downwelling on the colder side (counter-clockwise eddy) as a response to the horizontal density gradient and strain rate. The front drifts from $x=0$ to $x=x_a$ or $x=x_b$. Gray curves are isopycnals, and the vertical coordinate (z) is positive upward.

and stretching rates appear out of phase (Fig. 11e). Then the thermocline moves upward, and as the influence of the clockwise eddy becomes dominant, the upwelling current slowly decelerates (Fig. 12d). The maximum strain rate (κ) occurs right before high vorticity rather than at the same time (Fig. 11e).

The rotary coefficient and stream function are nearly in phase except when both stream function and velocity potential have weak fluctuations (Fig. 12c), which shows the rotation derived from surface currents is well aligned with vertical current rotation. These exhibit covariant subinertial currents at the surface and in the subsurface water column in a nearshore environment.

The local winds at SIO and TJR are not likely to be directly related to up/downward movements of the thermocline associated with wind-driven upwelling and downwelling (Fig. 12e). The wind in this region is relatively weak (a typical wind speed is 2–4 m s^{-1}) compared other regions on the U.S. West Coast. Therefore the integrated observations in this study are more appropriate to interpret with submesoscale process rather than classic Ekman dynamics.

4.5. PDFs of kinematic and dynamic quantities

As shown in Figs. 11 and 12, stream function, velocity potential, vorticity, and divergence are not always in-phase and out of phase with each other. However, paired quantities, stream function and vorticity and velocity potential and divergence, are linearly in-phase for most cases (Figs. 13a and b). In this study, high strain rate does not guarantee large vorticity (Figs. 11c and d), which differs from arguments in other submesoscale process literatures (e.g., Mahadevan and Tandon, 2006; Thomas et al., 2009).

The OW parameter ($g=\kappa^2-\zeta^2$) indicates the strain-dominated ($g>0$) and vorticity-dominated ($g<0$) region. Coherent eddies with clockwise and counter-clockwise rotations appear in the region of negative value ($g<0$) (e.g., Isern-Fontanet et al., 2004, 2006; Morrow et al., 2004; Chelton et al., 2007). However, both strain-dominated and vorticity-dominated coherent eddy structures were identified in this analysis (Fig. 13c).

5. Discussion and conclusion

Submesoscale eddies, characterized by 5–25 km diameters and 0.2–2 Rossby number, off southern San Diego are examined with

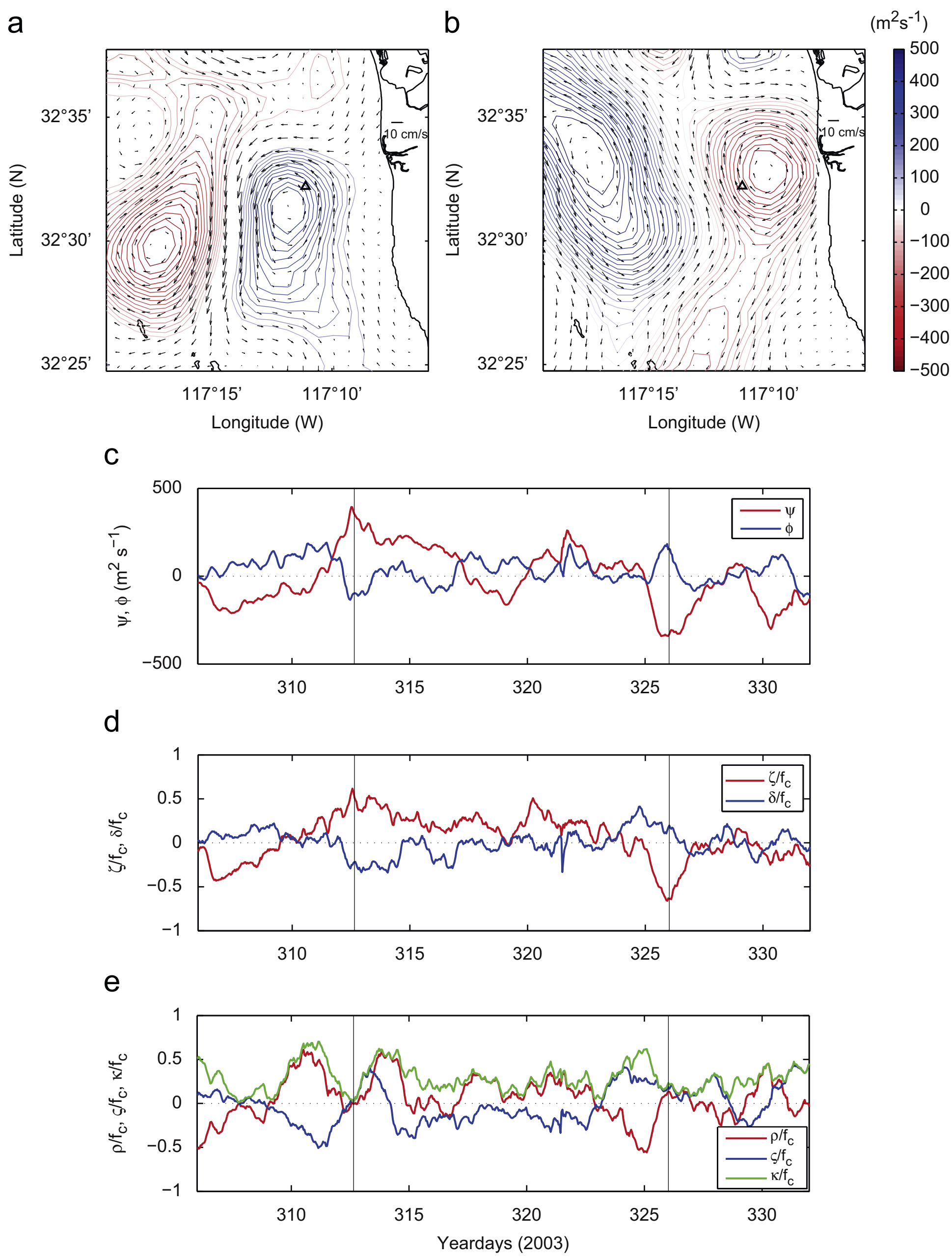

Fig. 11. Vertical structure (Part I). (a) and (b): Two snapshots of stream function when counter-clockwise and clockwise eddies pass by a local mooring marked as a black triangle on 312.65 and 326.02 yeardays of 2003 (GMT), respectively, which are indicated by two vertical black lines in (c)–(d) and Fig. 12. The stream function-derived surface currents ($\mathbf{u}_\psi$) are overlaid on the contours of stream function. (c) Stream function (ψ, m^2 s^{-1}) and velocity potential (ϕ, m^2 s^{-1}). (d) Normalized divergence (δ/f_c) and vorticity (ζ/f_c). (e) Normalized shearing rate (ϱ/f_c), stretching rate (ς/f_c), and strain rate (κ/f_c). (c)–(e) are values at the mooring location [a black triangle in (a) and (b)].

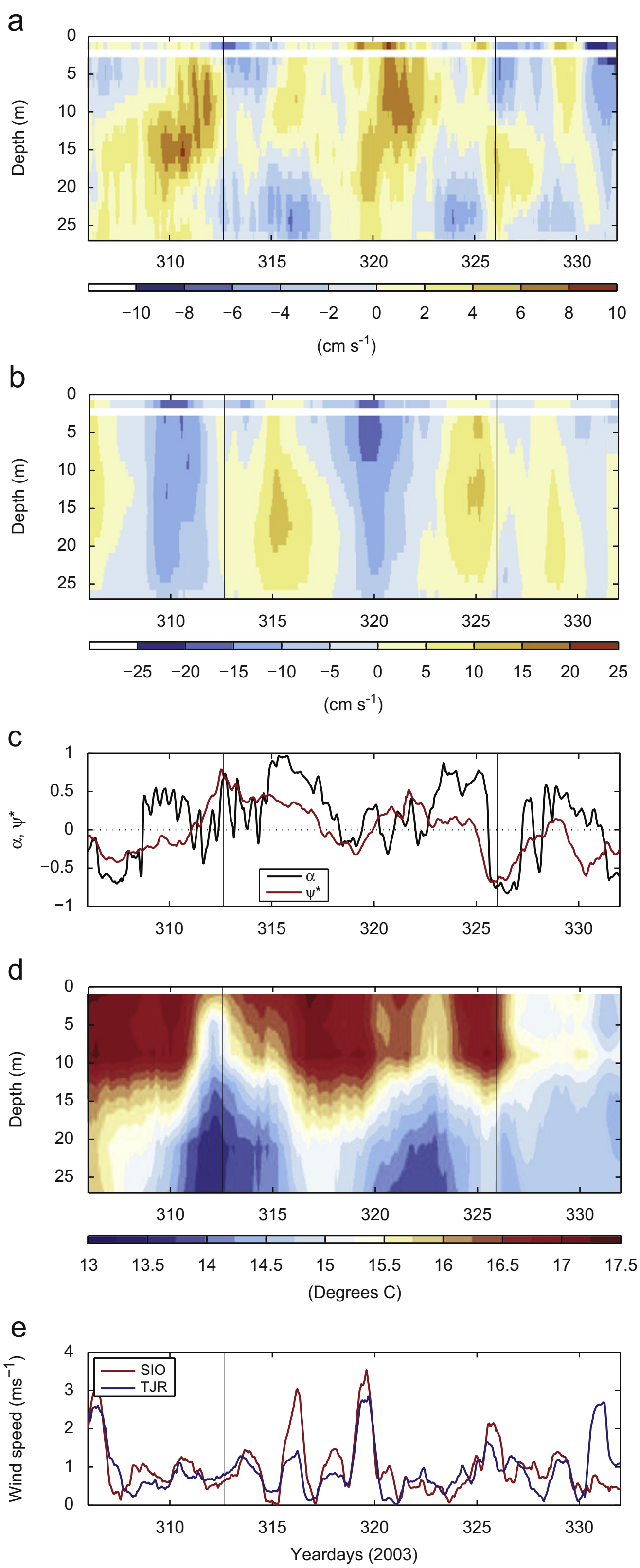

Fig. 12. Vertical structure (Part II). (a) and (b): Subinertial current profile (u- and v-components). The HF radar-derived surface currents are placed on the top of subsurface current profile (cm s^{-1}). (c) Vertical rotary coefficient [α in Eq. (25)] and normalized stream function ($\psi^* = \psi/\psi_0$, $\psi_0 = 500\,\mathrm{m^2\,s^{-1}}$). The negative and positive rotary coefficients denote the current profile with clockwise and counter-clockwise rotations, respectively, looking down from the top. (d) Subinertial temperature profile (°C). (e) Subinertial wind speed (m s^{-1}) at SIO and TJR.

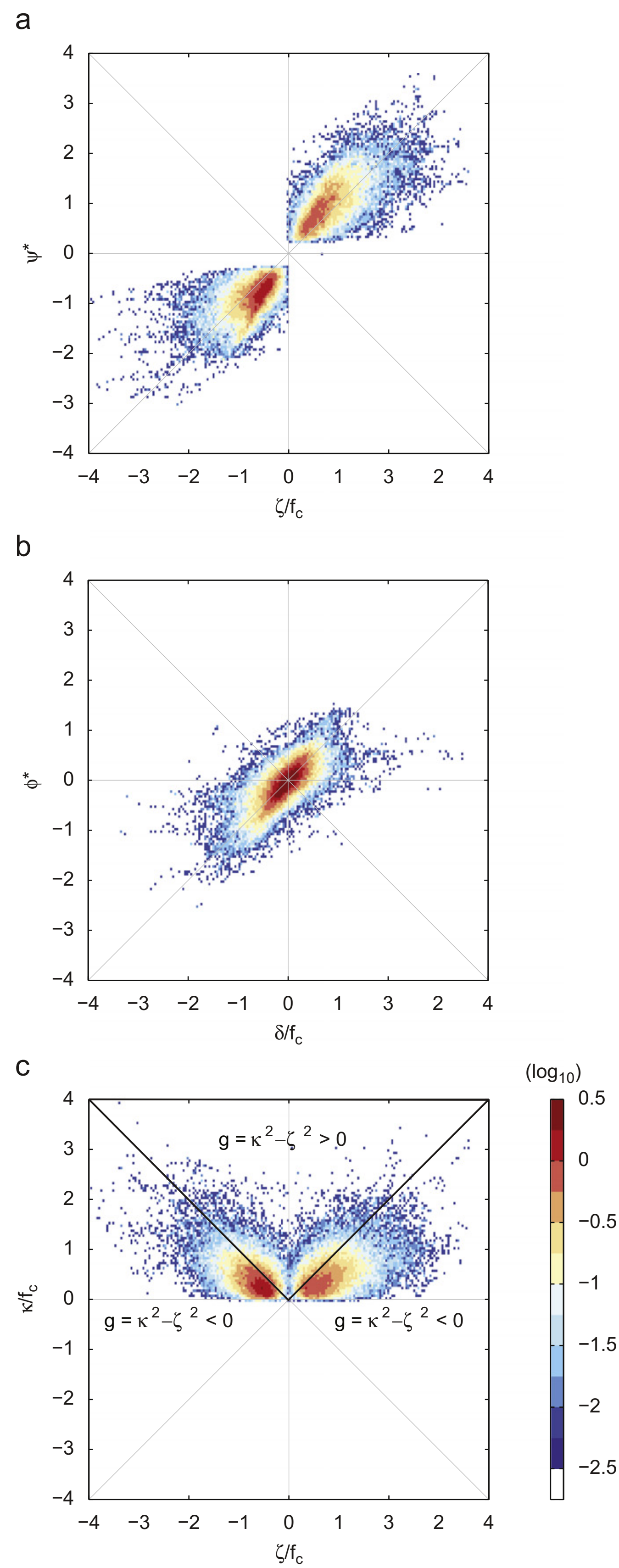

Fig. 13. Two-dimensional PDFs ($\log_{10}$ scale) of kinematic and dynamic quantities at the center of eddies. (a) ζ/f_c and ψ^* ($\psi^* = \psi/\psi_0$, $\psi_0 = 500\,\mathrm{m^2\,s^{-1}}$). (b) δ/f_c and ϕ^* ($\phi^* = \phi/\phi_0$, $\phi_0 = 500\,\mathrm{m^2\,s^{-1}}$). (c) ζ/f_c and κ/f_c. The area to satisfy the Okubo–Weiss criteria is indicated in (c).

high-frequency radar-derived subinertial surface currents. The kinematic and dynamic quantities — velocity potential, stream function, divergence, vorticity, and deformation rates — are directly estimated from radial velocity maps using optimal interpolation without passing through an error-prone vector current mapping stage. About 700 eddies with at least one-day persistence are identified from surface current data for two years, both clockwise and counter-clockwise. Eddies persist for 1–7 days, with weak seasonality, and migrate with a translation speed of 4–15 cm s^{-1} advected by background currents. They show a spatial preference according to the rotation. The horizontal structure within surface eddies has nearly symmetric tangential velocity and non-zero radial velocity. While the vorticity has a Gaussian shape with highest value at the center, the divergence appears as a weak variation across the eddy. Two episodic events of submesoscale eddies observed with a nearshore mooring reveal the frontal-scale secondary circulation. The vertical fluctuation of thermoclines is observed with an intense vertical velocity at the periphery of the submesoscale eddy.

For eddy identification, the winding-angle method is applied to optimally interpolated streamlines, which have more smooth spatial structure and less noisy estimates compared with vorticity. A cluster of nearly enclosed streamlines with persistent vorticity consist of an eddy time series. A threshold persistence is used to filter out the noise and error in the observations and an automated eddy detection technique. Since this applied approach is based on flow geometry, both strain-dominated and vorticity-dominated eddies were detected. The circulation within the eddy is nearly conserved, which shows physical consistency of the chosen technique. The estimated stream functions are likely to be matched with satellite remote sensing data (total suspended matter and Chlorophyll-a images, not shown).

The potential driving forces of eddies can be inferred from their generation, migration, and decay embedded in subinertial surface circulation. First, geophysical factors — coastline (e.g., capes, headlands, and bays) and bottom topography — are considered as a primary source. Surface circulation off southern San Diego is characterized with two major flows in a range of 20–30 cm s^{-1}: A seasonal southeastward flow which passes through the study domain diagonally yields horizontal shear. This shear causes clockwise and counter-clockwise flows, respectively, in the north and south of the TJR. The other is the flow sliding over Point La Jolla and Point Loma, which can generate eddies ($L<10$ km) off Mission Beach and near San Diego Bay mouth. A bifurcated flow near the TJR as upcoast and downcoast flows is frequently observed as filaments or tongues in remote sensing observations. Second, the spatial gradient of the wind field under moderate wind speeds (~ 3 m s^{-1}) is closely related to the generation of submesoscale eddies (e.g., Oey, 1996; Chavanne et al., 2002; Roughan et al., 2005). Those factors are strongly activated in the presence of horizontal density gradient, fronts, and filaments.

Submesoscale process studies have benefited from numerical models to explain four-dimensional dynamical components in a theoretical framework (e.g., Mahadevan and Tandon, 2006; Capet et al., 2008a; Thomas et al., 2009). However, there are very limited in situ observations because of the requirement for high-resolution (hourly in time and km in space) measurements of ocean surface and interior. As a part of the observational efforts, surface current measurements using high-frequency radar can provide a rich asset to substantiate the surface submesoscale process (e.g., fronts, filaments, and eddies) and to find the missing link between offshore and nearshore where satellite remote sensing observations are limited. On the top of that, the integrated observations with continuous time and broad spatial scales enable us to understand and interpret the real phenomena themselves (e.g., Stommel, 1989; Ocean.US, 2002).

Acknowledgments

Author is supported by the Coastal Ocean Currents Monitoring Program (COCMP) from the State of California, the Office of Naval Research (ONR), and the British Petroleum (BP) through the BP Institute at Scripps Institution of Oceanography (SIO). Surface current data are provided from the Southern California Coastal Ocean Observing System (SCCOOS, Available online at http://www.sccoos.org) at SIO. Author appreciates discussion and supports from Bruce Cornuelle, Eric Terrill, Mark Otero, Lisa Hazard, Paul Reuter, Jen Bowen, and Tom Cook at SIO.

Appendix A. Parameterizations

The covariance matrix between velocity potential (or stream function) ($\langle \xi\xi^\dagger \rangle$) and surface currents ($\langle \mathbf{uu}^\dagger \rangle$) is explored with model currents described with finite spectral basis, i.e., normal mode basis. The data ($\mathbf{d}$) in the physical space ($\mathbf{x}$) would be expressed with the trigonometric basis ($\mathbf{G}$) and their coefficients ($\mathbf{m}$) in the wavenumber space ($\mathbf{k}$):

$$\mathbf{d}(\mathbf{x}) = \sum_{\mathbf{k}} \mathbf{m}(\mathbf{k})\exp(i\mathbf{k}\cdot\mathbf{x}) = \mathbf{Gm}. \tag{A.1}$$

The covariance matrix of model currents is

$$\langle \mathbf{d}(\mathbf{x}_1)\mathbf{d}(\mathbf{x}_2)^\dagger \rangle = \sum_{\mathbf{k}_1}\sum_{\mathbf{k}_2} \langle \mathbf{m}(\mathbf{k}_1)\mathbf{m}(\mathbf{k}_2)^\dagger \rangle \exp[i(\mathbf{k}_1\cdot\mathbf{x}_1 - \mathbf{k}_2\cdot\mathbf{x}_2)], \tag{A.2}$$

where $\mathbf{k}=(k,l)$ and $\mathbf{x}=(x,y)$. † and $\cdot$ denote the complex conjugate transpose and the vector product, respectively. If the covariance matrix is stationary,

$$\langle \mathbf{d}(\mathbf{x}_1)\mathbf{d}(\mathbf{x}_2)^\dagger \rangle = \mathrm{cov}(\mathbf{x}_1 - \mathbf{x}_2), \tag{A.3}$$

then

$$\langle \mathbf{m}(\mathbf{k}_1)\mathbf{m}(\mathbf{k}_2)^\dagger \rangle = \sigma^2(\mathbf{k}_1)\delta(\mathbf{k}_1 - \mathbf{k}_2), \tag{A.4}$$

where $\delta(\mathbf{k})$ is the Dirac delta function in the wavenumber space. The covariance matrix is presented as a function spatial lag ($\Delta\mathbf{x}$)

$$\mathrm{cov}(\Delta\mathbf{x}) = \sum_{\mathbf{k}} \sigma^2(\mathbf{k})\exp(i\mathbf{k}\cdot\Delta\mathbf{x}) = \mathbf{G}\langle \mathbf{mm}^\dagger \rangle, \tag{A.5}$$

where $\Delta\mathbf{x} = \mathbf{x}_1 - \mathbf{x}_2$. This is a conversion of the covariance matrix from four-dimensional covariance matrix of a given quantity to two-dimensional covariance matrix using its power spectral density and trigonometric basis functions. The spatial derivation of model currents is

$$\frac{\partial \mathbf{d}}{\partial \mathbf{x}} = \mathbf{Gkm}, \tag{A.6}$$

and the covariance matrix is computed in a similar way:

$$\left\langle \frac{\partial \mathbf{d}(\mathbf{x}_1)}{\partial \mathbf{x}_1} \frac{\partial \mathbf{d}(\mathbf{x}_2)}{\partial \mathbf{x}_2}^\dagger \right\rangle = \sum_{\mathbf{k}_1}\sum_{\mathbf{k}_2} \langle [\mathbf{k}_1\mathbf{m}(\mathbf{k}_1)][\mathbf{k}_2\mathbf{m}(\mathbf{k}_2)]^\dagger \rangle \times \exp[i(\mathbf{k}_1\cdot\mathbf{x}_1 - \mathbf{k}_2\cdot\mathbf{x}_2)]. \tag{A.7}$$

The coefficients are simply expressed as

$$\langle [\mathbf{k}_1\mathbf{m}(\mathbf{k}_1)][\mathbf{k}_2\mathbf{m}(\mathbf{k}_2)]^\dagger \rangle = \mathbf{k}_1^2\sigma^2(\mathbf{k}_1)\delta(\mathbf{k}_1 - \mathbf{k}_2). \tag{A.8}$$

A.1. Data-data covariance matrix

Both velocity potential and stream function are parameterized with trigonometric basis functions ($\mathbf{m}_\phi$,$\mathbf{m}_\psi$):

$$\phi(\mathbf{x}) = \sum_{\mathbf{k}} \mathbf{m}_\phi(\mathbf{k})\exp(i\mathbf{k}\cdot\mathbf{x}) = \mathbf{G}\mathbf{m}_\phi, \tag{A.9}$$

$$\psi(\mathbf{x}) = \sum_{\mathbf{k}} \mathbf{m}_\psi(\mathbf{k})\exp(i\mathbf{k}\cdot\mathbf{x}) = \mathbf{G}\mathbf{m}_\psi. \tag{A.10}$$

From the relationship between the power spectral density in the wavenumber space and the covariance matrix in the physical domain [Eq. (A.5)], the covariance matrices of velocity potential and stream function are

$$\mathrm{cov}_{\phi\phi}(\Delta\mathbf{x}) = \mathbf{G}\langle \mathbf{m}_\phi \mathbf{m}_\phi^\dagger \rangle, \tag{A.11}$$

$$\mathrm{cov}_{\psi\psi}(\Delta\mathbf{x}) = \mathbf{G}\langle \mathbf{m}_\psi \mathbf{m}_\psi^\dagger \rangle, \tag{A.12}$$

and

$$\mathrm{cov}_{\phi\psi}(\Delta\mathbf{x}) = 0. \tag{A.13}$$

The covariance matrices of current components are

$$\mathrm{cov}_{uu}(\Delta\mathbf{x}) = \mathrm{cov}_{u_\phi u_\phi}(\Delta\mathbf{x}) + \mathrm{cov}_{u_\psi u_\psi}(\Delta\mathbf{x}), \tag{A.14}$$

$$\mathrm{cov}_{vv}(\Delta\mathbf{x}) = \mathrm{cov}_{v_\phi v_\phi}(\Delta\mathbf{x}) + \mathrm{cov}_{v_\psi v_\psi}(\Delta\mathbf{x}), \tag{A.15}$$

and

$$\mathrm{cov}_{uv}(\Delta\mathbf{x}) = \mathrm{cov}_{u_\phi v_\phi}(\Delta\mathbf{x}) + \mathrm{cov}_{u_\psi v_\psi}(\Delta\mathbf{x}), \tag{A.16}$$

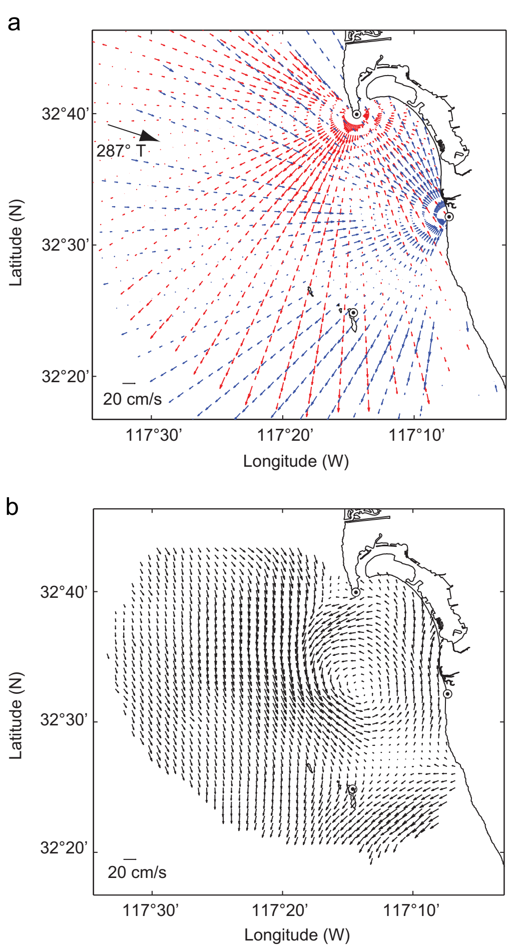

Fig. B1. An example of the subinertial (a) radial velocity map and (b) vector current map at June 1, 2003, 18:00 (GMT). The red and blue colors denote radial velocities from SDPL and SDBP, respectively, The SDCI site was temporarily shutdown at that time. The excluded azimuthal bin at 287° from true North (SDBP) was indicated in (a). (For interpretation of the references to color in this figure legend, the reader is referred to the web version of this article.)

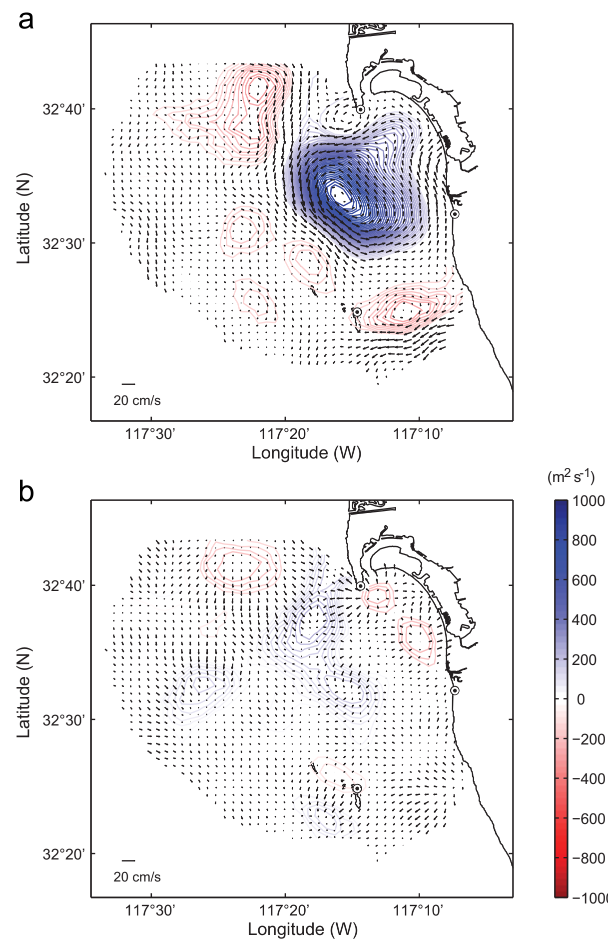

Fig. B2. (a) Stream function (ψ, $\mathrm{m^2\,s^{-1}}$) and (b) velocity potential (ϕ, $\mathrm{m^2\,s^{-1}}$) directly estimated from radial velocities using optimal interpolation, shown with superposed vector currents of corresponding components ($\mathbf{u}_\psi$ and $\mathbf{u}_\phi$), respectively. Blue areas indicate counter-clockwise or downwelling, and red areas indicate clockwise or upwelling. (For interpretation of the references to color in this figure legend, the reader is referred to the web version of this article.)

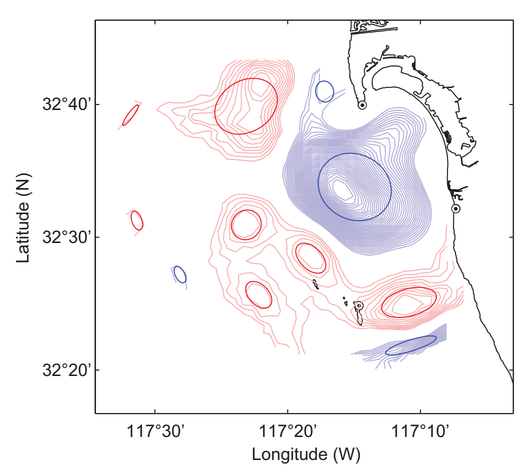

Fig. B3. A set of streamlines detected by the winding angle (WA) method and the fitted ellipses. Blue and red areas (or ellipses) indicate counter-clockwise and clockwise, respectively. (For interpretation of the references to color in this figure legend, the reader is referred to the web version of this article.)

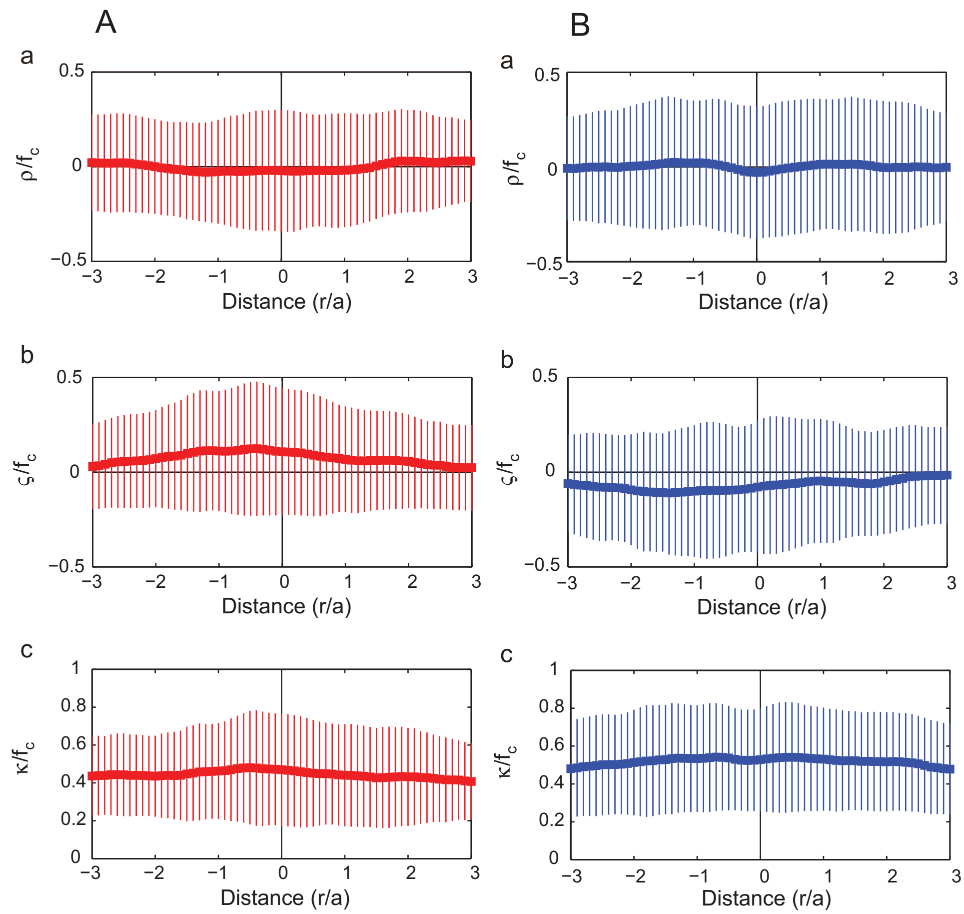

Fig. B4. Horizontal structure of submesoscale eddies along the major axis (r/a) is presented as a function of distance from the center. The mean and rms are indicated as squares and error bars, respectively. Column A: clockwise eddies. Column B: counter-clockwise eddies. (a) Shearing deformation rate (ϱ/f_c). (b) Stretching deformation rate (ς/f_c). (c) Strain rate (κ/f_c).

where

$$\mathrm{cov}_{u_\phi u_\phi}(\Delta\mathbf{x}) = \mathbf{G}\langle (ik\mathbf{m}_\phi)(ik\mathbf{m}_\phi)^\dagger \rangle, \tag{A.17}$$

$$\mathrm{cov}_{u_\psi u_\psi}(\Delta\mathbf{x}) = \mathbf{G}\langle (-il\mathbf{m}_\psi)(-il\mathbf{m}_\psi)^\dagger \rangle, \tag{A.18}$$

$$\mathrm{cov}_{v_\phi v_\phi}(\Delta\mathbf{x}) = \mathbf{G}\langle (il\mathbf{m}_\phi)(il\mathbf{m}_\phi)^\dagger \rangle, \tag{A.19}$$

$$\mathrm{cov}_{v_\psi v_\psi}(\Delta\mathbf{x}) = \mathbf{G}\langle (ik\mathbf{m}_\psi)(ik\mathbf{m}_\psi)^\dagger \rangle, \tag{A.20}$$

$$\mathrm{cov}_{u_\phi v_\phi}(\Delta\mathbf{x}) = \mathbf{G}\langle (ik\mathbf{m}_\phi)(il\mathbf{m}_\phi)^\dagger \rangle, \tag{A.21}$$

and

$$\mathrm{cov}_{u_\psi v_\psi}(\Delta\mathbf{x}) = \mathbf{G}\langle (-il\mathbf{m}_\psi)(ik\mathbf{m}_\psi)^\dagger \rangle. \tag{A.22}$$

A.2. Data-model covariance matrix

The covariance matrices between velocity potential (or stream function) and its corresponding current components are

$$\mathrm{cov}_{u_\phi \phi}(\Delta\mathbf{x}) = \mathbf{G}\langle (ik\mathbf{m}_\phi)\mathbf{m}_\phi^\dagger \rangle, \tag{A.23}$$

$$\mathrm{cov}_{v_\phi \phi}(\Delta\mathbf{x}) = \mathbf{G}\langle (il\mathbf{m}_\phi)\mathbf{m}_\phi^\dagger \rangle, \tag{A.24}$$

$$\mathrm{cov}_{u_\psi \psi}(\Delta\mathbf{x}) = \mathbf{G}\langle (-il\mathbf{m}_\psi)\mathbf{m}_\psi^\dagger \rangle, \tag{A.25}$$

and

$$\mathrm{cov}_{v_\psi \psi}(\Delta\mathbf{x}) = \mathbf{G}\langle (ik\mathbf{m}_\psi)\mathbf{m}_\psi^\dagger \rangle. \tag{A.26}$$

Appendix B. Sequential procedure of eddy detection

A sequential procedure to detect eddies from HF radar-derived radial velocity maps is described. Fig. B1a shows a snapshot of daily averaged radial velocity maps from SDPL (red) and SDBP (blue) sites. The SDCI site was temporarily shutdown at that time, and the radial velocities at an azimuthal bin of SDBP site (287° from true north in clockwise) are excluded. Using OI, the vector currents, stream function, and velocity potential are estimated (Figs. B1b, B2a, and B2b). The current components corresponding to stream function (u_ψ and v_ψ) and velocity potential (u_ϕ and v_ϕ) are overlaid on each map. The red and blue colors indicate clockwise (convergence) and counter-clockwise (divergence) flow as the sign convention of stream function (velocity potential). The co-centered streamlines are identified with the WA method (Section 3), and they are fitted with ellipses (Fig. B3).

References

Aref, H., 1983. Integrable chaotic and turbulent vortex motion in two-dimensional flows. Annu. Rev. Fluid Mech. 15, 345–389. doi:10.1146/annurev.fl.15.010183.002021.

Arfken, G.B., Weber, H.J., 1995. Mathematical Methods for Physicists, fourth ed. Academic Press.

Basdevant, C., Philipovitch, T., 1994. On the validity of the Weiss criterion in two-dimensional turbulence. Physica D 73, 17–30.

Beckenbach, E., Washburn, L., 2004. Low-frequency waves in the Santa Barbara Channel observed by high-frequency radar. J. Geophys. Res. 109, C02010. doi:10.1029/2003JC001999.

Bijlsma, S.J., Hafkenscheid, L.M., Lynch, P., 1986. Computation of the stream function and velocity potential and reconstruction of the wind field. Mon. Weather Rev. 114, 1547–1551.

Bonnet, J.P., Glauser, M.N., 1993. Eddy Structure Identification in Free Turbulent Shear Flows. Fluid Mechanics and its Applications, vol. 21. Kluwer Academic Publishers.

Brassington, G.B., 2009. Estimating surface divergence of ocean eddies using observed trajectories from a surface drifting buoy. J. Atmos. Ocean. Technol. 27, 705–720. doi:10.1175/2009JTECHO651.1.

Caldeira, R.M.A., Marchesiello, P., Nezlin, N.P., DiGiacomo, P.M., McWilliams, J.C., 2005. Island wakes in the Southern California Bight. J. Geophys. Res. 110, C11012. doi:10.1029/2004JC002675.

Capet, X., McWilliams, J.C., Molemaker, M.J., Shchepetkin, A.F., 2008a. Mesoscale to submesoscale transition in the California Current System. Part I: flow structure, eddy flux, and observational tests. J. Phys. Oceanogr. 38 (1), 29–43. doi:10.1175/2007JPO3671.1.

Capet, X., McWilliams, J.C., Molemaker, M.J., Shchepetkin, A.F., 2008b. Mesoscale to submesoscale transition in the California current system. Part II: frontal processes. J. Phys. Oceanogr. 38 (1), 44–64. doi:10.1175/2007JPO3672.1.

Chaigneau, A., Gizolme, A., Grado, C., 2008. Mesoscale eddies off Peru in altimeter records: identification algorithm and eddy spatio-temporal patterns. Progr. Oceanogr. 79, 106–119. doi:10.1016/j.pocean.2008.10.013.

Chavanne, C., Flament, P., Lumpkin, R., Dousset, B., Bentamy, A., 2002. Scatterometer observations of wind variations induced by oceanic islands: implications for wind-driven ocean circulation. Can. J. Remote Sens. 28 (3), 466–474.

Chelton, D.B., Schlax, M.G., Samelson, R.M., de Szoeke, R.A., 2007. Global observations of large oceanic eddies. Geophys. Res. Lett. 34, L15606. doi:10.1029/2007GL030812.

Cho, K., Reid, R., Nowlin Jr., W.D., 1998. Objectively mapped stream function fields on the Texas–Louisiana shelf based on 32 months of moored current meter data. J. Geophys. Res. 103 (C5), 10377–10390.

Coulliette, C., Lekien, F., Paduan, J.D., Haller, G., Marsden, J.E., 2007. Optimal pollution mitigation in Monterey Bay based on coastal radar data and nonlinear dynamics. Environ. Sci. Technol. 41 (41), 6562–6572. doi:10.1021/es0630691.

Davies, P.A., Dakin, J.M., Falconer, R.A., 1995. Eddy formation behind a coastal headland. J. Coastal Res. 11 (1), 154–167.

DiGicomo, P.M., Holt, B., 2001. Satellite observations of small coastal ocean eddies in the Southern California Bight. J. Geophys. Res. 106 (C10), 22521–22543.

Ebisuzaki, W., 1997. A method to estimate the statistical significance of a correlation when the data are serially correlated. J. Climate 10(9), 2147–2153.

Ebling, J., Scheuermann, G., 2003. Clifford convolution and pattern matching on vector fields. IEEE Visualization VIS 2003, 193–200.

Garrett, C., Munk, W., 1979. Internal waves in the ocean. Annu. Rev. Fluid Mech. 11, 339–369.

Glenn, S.M., Forristall, G.Z., Cornillon, P., Milkowski, G., 1990. Observations of Gulf Stream Ring 83-E and their interpretation using feature models. J. Geophys. Res. 95 (C8), 13043–13063.

Guo, D., 2004. Automated feature extraction in oceanographic visualization. Master's Thesis, Massachusetts Institute of Technology.

Guo, D., Evangelinos, C., Patrikalakis, N.M., 2004. Flow feature extraction in oceanographic visualization. In: Computer Graphics International Conference, IEEE Computer Society Press, Greece, pp. 162–173.

Heiberg, E., Ebbers, T., Wigström, L., Karlsson, M., 2003. Three-dimensional flow characterization using vector pattern matching. IEEE Trans. Visualization Comput. Graph. 9 (3), 313–319.

Higgins, K., Rutten, M., Ooi, A., Chong, M.S., 2009. The interaction of counter-rotating strained vortex pairs with a third vortex. Fluid Dyn. Res. 41, 1–24. doi:10.1088/0169-5983/41/3/035502.

Hoskins, B., Bretherton, F., 1972. Atmospheric frontogenesis models: mathematical formulation and solution. J. Atmos. Sci. 29 (1), 11–37.

Hubertz, J.M., Garcia, A.W., Reid, R.O., 1972. Objective analysis of oceanic surface currents. In: Contribution on the Physical Oceanography of the Gulf of Mexico. Gulf Publishing Co, Houston, TX, pp. 139–148 (Chapter 7).

Hwang, C., Wu, C.-R., Kao, R., 2004. TOPEX/Poseidon observations of mesoscale eddies over the subtropical countercurrent: kinematic characteristics of an anticyclonic eddy and a cyclonic eddy. J. Geophys. Res. 109, C08013. doi:10.1029/2003JC002026.

Ingram, R.G., Chu, V.H., 1987. Flow around islands in Rupert Bay: an investigation of the bottom friction effect. J. Geophys. Res. 92 (C13), 14521–14533.

Isern-Fontanet, J., Font, J., Garcia-Ladona, E., Emelianov, M., Millot, C., Taupier-Letage, I., 2004. Spatial structure of anticyclonic eddies in the Algerian basin (Mediterranean Sea) analyzed using the Okubo–Weiss parameter. Deep Sea Res. 51, 3009–3028. doi:10.1016/j.dsr2.2004.09.013.

Isern-Fontanet, J., Garcia-Radona, E., Font, J., 2006. Vortices of the mediterranean sea: an altimetric perspective. J. Phys. Oceanogr. 36, 87–103.

Jeong, J., Hussain, E., 1995. On the identification of a vortex. J. Fluid Mech. 285, 69–94.

Kaplan, D.M., Lekein, F., 2007. Spatial interpolation and filtering of surface current data based on open-boundary modal analysis. J. Geophys. Res. 112, C12007. doi:10.1029/2006JC003984.

Kim, S.Y., 2009. Coastal ocean studies in southern San Diego using high-frequency radar derived surface currents. Ph.D. Thesis, Scripps Institution of Oceanography Technical Report 〈http://escholarship.org/uc/item/2z5660f4〉.

Kim, S.Y., Terrill, E.J., Cornuelle, B.D., 2007. Objectively mapping HF radar-derived surface current data using measured and idealized data covariance matrices. J. Geophys. Res. 112, C06021. doi:10.1029/2006JC003756.

Kim, S.Y., Terrill, E.J., Cornuelle, B.D., 2008. Mapping surface currents from HF radar radial velocity measurements using optimal interpolation. J. Geophys. Res. 113, C10023. doi:10.1029/2007JC004244.

Klein, P., Lapeyre, G., 2009. The oceanic vertical pump induced by mesoscale and submesoscale turbulence. Annu. Rev. Mar. Sci. 1, 351–375. doi:10.1146/annurev.marine.010908.163704.

Lapeyre, G., Klein, P., 2006. Impact of the small-scale elongated filaments on the oceanic vertical pump. J. Mar. Res. 64 (6), 835–851.

Leaman, K.D., Sanford, T.B., 1975. Vertical energy propagation of inertial waves: a vector spectral analysis of velocity profiles. J. Geophys. Res. 80 (15), 1975–1978.

Lekien, F., Gildor, H., 2009. Computation and approximation of the length scales of harmonic modes with application to the mapping of surface current in the Gulf of Eilat. J. Geophys. Res. 114, C06024. doi:10.1029/2008JC004742.

Levy, M., Klein, P., Treguier, A.-M., 2001. Impact of sub-mesoscale physics on production and subduction of phytoplankton in an oligotrophic regime. J. Mar. Res. 59 (4), 535–565.

Li, Z., Chao, Y., McWilliams, J.C., 2006. Computation of the streamfunction and velocity potential for limited and irregular domains. Mon. Weather Rev. 134, 3384–3394.

Lipphardt Jr., B.L., Kirwan Jr., A.D., Grosch, C.E., Lewis, J.K., Paduan, J.D., 2000. Blending HF radar and model velocities in Monterey Bay through normal mode analysis. J. Geophys. Res. 105 (C2), 3425–3450.

Mahadevan, A., Tandon, A., 2006. An analysis of mechanism for submesoscale vertical motion at ocean fronts. Ocean Model. 14, 241–256. doi:10.1016/j.ocemod.2006.05.006.

Mahadevan, A., Thomas, L.N., Tandon, A., 2008. Comment on "Eddy/Wind interactions stimulate extraordinary Mid-Ocean plankton blooms". Science 320 (5875), 448b. doi:10.1126/science.1152111.

Martin, A.P., Richards, K.J., 2001. Mechanisms for vertical nutrient transport within a North Atlantic mesoscale eddy. Deep-Sea Res. II 48 (4–5), 757–773. doi:10.1016/S0967-0645(00)00096-5.

McGillicuddy, D.J., Anderson, L.A., Bates, N.R., Bibby, T., Buesseler, K.O., Carlson, C.A., Davis, C.S., Ewart, C., Falkowski, P.G., Goldthwait, S.A., Hansell, D.A., Jenkins, W.J., Johnson, R., Kosnyrev, V.K., Ledwell, J.R., Li, Q.P., Siegel, D.A., Steinberg, D.K., 2007. Eddy/wind interactions stimulate extraordinary mid-ocean plankton blooms. Science 316 (5827), 1021.

McWilliams, J.C., 1984. The emergence of isolated coherent vortices in turbulent flow. J. Fluid Mech. 146, 21–43.

McWilliams, J.C., 1985. Submesoscale, coherent vortices in the ocean. J. Geophys. Res. 23 (2), 162–182.

McWilliams, J.C., 1990. The vortices of two-dimensional turbulence. J. Fluid Mech. 219, 361–385.

Morrow, R., Birol, F., Griffin, D., Sudre, J., 2004. Divergent pathways of cyclonic and anti-cyclonic ocean eddies. Geophys. Res. Lett. 31, L24311. doi:10.1029/2004GL020974.

Munk, W., Armi, L., Fischer, K., Zachariasen, F., 2000. Spirals on the sea. Proc. R. Soc. London A 456, 1217–1280.

Nencioli, F., Dong, C., Dickey, T., Washburn, L., McWilliams, J.C., 2010. A vector geometry based eddy detection algorithm and its application to a high-resolution numerical model product and high-frequency radar surface velocities in the Southern California Bight. J. Atmos. Ocean. Technol. 27, 564–579. doi:10.1175/2009JTECHO725.1.

Nurser, A.J.G., Zhang, J.W., 2000. Eddy-induced mixed layer shallowing and mixed layer/thermocline exchange. J. Geophys. Res. 105 (C9), 21851–21868.

Nybelen, L., Paoli, R., 2009. Direct and large-eddy simulations of merging in corotating vortex system. AIAA J. 47 (1), 157–167. doi:10.2514/1.38026.

Ocean.US, 2002. An Integrated and Sustained Ocean Observing System (IOOS) for the United States: Design and Implementation. Technical Report, Arlington, VA.

Oey, L.-Y., 1996. Flow around a coastal bend: a model of the Santa Barbara Channel eddy. J. Geophys. Res. 101 (C7), 16667–16682.

Oey, L.-Y., Wang, D.-P., Hayward, T., Winant, C., Hendershott, M., 2001. Upwelling and cyclonic regimes of the near-surface circulation in the Santa Barbara Channel. J. Geophys. Res. 106 (C5), 9213–9222.

Okubo, A., 1970. Horizontal dispersion of floatable particles in the vicinity of velocity singularities such as convergences. Deep Sea Res. 17, 445–454.

Pattiaratchi, P., James, A., Collins, M., 1986. Island wakes and headland eddies: a comparison between remotely sensed data and laboratory experiments. J. Geophys. Res. 92 (C1), 783–794.

Pawlak, G., MacCready, P., Edwards, K.A., McCabe, R., 2003. Observations on the evolution of tidal vorticity at stratified deep water headland. Geophys. Res. Lett. 30 (24), 2234. doi:10.1029/2003GL018092.

Pollard, R., Regier, L., 1992. Vorticity and vertical circulation at an ocean front. J. Phys. Oceanogr. 22 (6), 609–625.

Pollard, R.T., Regier, L., 1990. Large variations in potential vorticity at small spatial scales in the upper ocean. Nature 348 (6298), 227–229. doi:10.1038/348227a0.

Portela, L.M., 1997. On the identification and classification of vortices. Ph.D. Thesis, Stanford University, School of Mechanical Engineering.

Roughan, M., Terrill, E.J., Largier, J.L., Otero, M.P., 2005. Observations of divergence and upwelling around Point Loma, California. J. Geophys. Res. 110, C04011. doi:10.1029/2004JC002662.

Sadarjoen, I.A., 1999. Extraction and visualization of geometries in fluid flow fields. Ph.D. Thesis, Delft University of Technology.

Sadarjoen, I.A., Post, F.H., 1999. Geometric methods for vortex extraction. IEEE Trans. Visualization Comput. Graph, 53–62.
Sanderson, B.G., 1995. Structure of an eddy measured with drifters. J. Geophys. Res. 100 (C4), 6761–6776.
Sathyendranath, S., Longhurst, A., Caverhill, C.M., Platt, T., 1995. Regionally and seasonally differentiated primary production in the North Atlantic. Deep-Sea Res. I 42 (10), 1773–1802. doi:10.1016/0967-0637(95)00059-F.
Shapiro, G.I., Barton, E.D., Meschanov, S.L., 1997. Capture and release of Lagrangian floats by eddies in shear flow. J. Geophys. Res. 102 (C13), 27887–27902.
Signell, R.P., Geyer, W.R., 1991. Transient eddy formation around headlands. J. Geophys. Res. 96, 2561–2575.
Spall, M., 1995. Frontogenesis, subduction, and cross-front exchange at upper ocean fronts. J. Geophys. Res. 100 (C2), 2543–2557.
Stommel, H., 1989. Why we are oceanographers. Oceanography 2 (2), 48–54.
Sujudi, D., 1995. Identification of swirling flow in 3-D vector fields. In: American Institute of Aeronautics and Astronautics. 12th AIAA Computational Fluid Dynamics Conference, pp. 792–799.
Taylor, G.I., 1918. On the dissipation of eddies. The Scientific Papers of Sir Geoffrey Ingram Taylor. Meteorology, Oceanography and Turbulent Flow, vol. 2. Cambridge University Press, Cambridge, England, UK, pp. 96–101.
Thomas, L.N., Tandon, A., Mahadevan, A., 2009. Submesoscale processes and dynamics. Ocean Modeling in an Eddying Regime. Geophysical Monograph Series, vol. 177. American Geophysical Union, Washington, DC, pp. 17–38.
Vatistas, G.H., 1998. New model for intense self-similar vortices. J. Propuls. Power 14 (4), 462–469.
Weiss, J.B., 1981. The dynamics of enstrophy transfer in two-dimensional hydrodynamics. Physica D 48, 273–294.
Wiebel, A., 2004. Feature detection in vector fields using the Helmholtz–Hodge decomposition. Master's Thesis, University of Kaiserslautern, Department of Computer Science.
Williams, R., Follows, M., 1998. Oceanography: eddies make ocean deserts bloom. Nature 394, 228–229.
Williams, R., Follows, M., 2003. Physical transport of nutrients and the maintenance of biological production. In: Ocean Biogeochemistry: The Role of the Ocean Carbon Cycle in Global Change. Springer (Chapter 2).
Wolanski, E., Imberger, J., Heron, M.L., 1984. Island wakes in shallow coastal waters. J. Geophys. Res. 89 (C6), 10553–10569.
Woods, J.D., 1980. Do waves limit turbulent diffusion in the ocean? Nature 288 219–224.
Woods, J.D., 1988. Mesoscale upwelling and primary production. In: Toward a Theory of Biological Physical Interactions in the World Ocean. Kluwer, pp. 7–38.
Wunsch, C., 1999. Where do ocean eddy heat fluxes matter? J. Geophys. Res. 104 (C6) 13235–13249.
Zhu, Z.F., Moorhead, R.J., 1995. Extracting and visualizing ocean eddies in time-varying flow fields. In: 7th International Conference on Flow Visualization, Seattle, WA, September.
Zimmerman, J.T.F., 1981. Dynamics diffusion and geomorphological significance of tidal residual eddies. Nature 290, 549–555.